

Mixture of Gaussian-distributed Prototypes with Generative Modelling for Interpretable and Trustworthy Image Recognition

Chong Wang, *Member, IEEE*, Yuanhong Chen, Fengbei Liu, Yuyuan Liu, Davis James McCarthy, Helen Frazer, and Gustavo Carneiro

Abstract—Prototypical-part methods, e.g., ProtoPNet, enhance interpretability in image recognition by linking predictions to training prototypes, thereby offering intuitive insights into their decision-making. Existing methods, which rely on a point-based learning of prototypes, typically face two critical issues: 1) the learned prototypes have limited representation power and are not suitable to detect Out-of-Distribution (OoD) inputs, reducing their decision trustworthiness; and 2) the necessary projection of the learned prototypes back into the space of training images causes a drastic degradation in the predictive performance. Furthermore, current prototype learning adopts an aggressive approach that considers only the most active object parts during training, while overlooking sub-salient object regions which still hold crucial classification information. In this paper, we present a new generative paradigm to learn prototype distributions, termed as **Mixture of Gaussian-distributed Prototypes** (MGProto). The distribution of prototypes from MGProto enables both interpretable image classification and trustworthy recognition of OoD inputs. The optimisation of MGProto naturally projects the learned prototype distributions back into the training image space, thereby addressing the performance degradation caused by prototype projection. Additionally, we develop a novel and effective prototype mining strategy that considers not only the most active but also sub-salient object parts. To promote model compactness, we further propose to prune MGProto by removing prototypes with low importance priors. Experiments on CUB-200-2011, Stanford Cars, Stanford Dogs, and Oxford-IIIT Pets datasets show that MGProto achieves state-of-the-art image recognition and OoD detection performances, while providing encouraging interpretability results. Code is available at <https://github.com/cwanganrun/MGProto>.

Index Terms—Interpretability, prototypical-part networks, Gaussian mixture, horse racing, generative modelling, prototype mining.

1 INTRODUCTION

DEEP learning models [1], [2] show remarkable performance in computer vision tasks, but their complex network architectures, high non-linearity, and massive parameter spaces make their decision processes opaque [3], [4]. As a result, deep learning models may not be trustworthy, par-

ticularly in safety-critical domains where the consequences of model errors can be severe [4], [5], [6], [7]. To alleviate this issue, explainable artificial intelligence (XAI) has gained increasing focus, striving to develop interpretable strategies to explain the internal workings of deep learning models in a manner comprehensible to humans [8], [9], [10], [11], [12]. Among them, the prototypical-part network (ProtoPNet) [10] is an appealing grey-box approach that classifies images based on similarities of the test sample to the prototypes corresponding to image patches previously-seen in the training set. Such strategy relies on train-test sample associations for decision making, which resembles how humans reason according to cognitive psychological studies [13], [14] revealing that humans use past cases as models when learning to solve problems. The success of ProtoPNet has motivated the development of its many variants, e.g., TesNet [15], ProtoTree [16], and PIP-Net [17].

Current prototypical part networks [10], [17], [18] depend on a discriminative classifier [19] optimised with point-based learning techniques that train prototypes with specific values. Such a classifier produces logits (computed from a weighted sum of similarity scores), which are passed on to a softmax function to directly obtain the class probability given an input image, i.e., $p(c|x)$, as shown in Fig. 1(a). Though straightforward and easy to implement, the resulting prototypes from point-based learning have limited representation power and tends to suffer from drastic performance degradation (see Fig. 2) upon the prototype

- Chong Wang and Yuanhong Chen are with the Australian Institute for Machine Learning (AIML), University of Adelaide, SA 5000, Australia. Chong Wang is also with the Department of Radiology, Stanford University, Stanford, CA 94305-5105, USA. E-mail: chong.wang@adelaide.edu.au; yuanhong.chen@adelaide.edu.au
- Fengbei Liu is with the School of Electrical and Computer Engineering, Cornell University and Cornell Tech, New York, NY 10044, USA. E-mail: fl453@cornell.edu
- Yuyuan Liu is with the Department of Engineering Science, University of Oxford, OX1 2JD Oxford, U.K. E-mail: yuyuan.liu@adelaide.edu.au
- Davis James McCarthy is with the St. Vincent's Institute of Medical Research, Melbourne, VIC 3065, Australia, and also with the Melbourne Integrative Genomics, The University of Melbourne, Melbourne, VIC 3010, Australia. E-mail: dmccarthy@svi.edu.au
- Helen Frazer is with the St Vincent's Hospital Melbourne, Melbourne, VIC 3002, Australia. E-mail: helen.frazer@svha.org.au
- Gustavo Carneiro is with the Centre for Vision, Speech and Signal Processing (CVSSP), University of Surrey, GU2 7XH Guildford, U.K., and also with the Australian Institute for Machine Learning (AIML), The University of Adelaide, Adelaide, SA 5000, Australia. E-mail: g.carneiro@surrey.ac.uk

This work was supported by the Australian Government under the Medical Research Future Fund for the Transforming Breast Cancer Screening with Artificial Intelligence (BRAIx) Project under Grant MRFAI000090 and the U.K. Engineering and Physical Sciences Research Council through Grant EP/Y018036/1. Chong Wang and Yuanhong Chen contributed equally to this work. (Corresponding author: Gustavo Carneiro.)

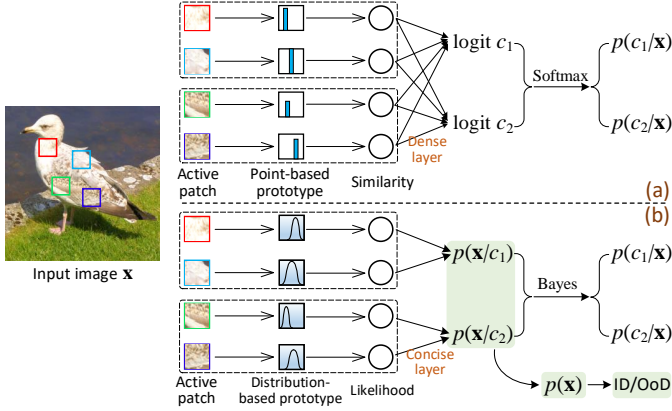


Fig. 1. (a) Current prototypical-part networks are softmax-based discriminative classifiers, forming a point-based learning of prototypes with limited representation power, which are challenged by the detection of OoD inputs. (b) Our method learns a mixture of Gaussian-distributed prototypes with a generative modelling, enabling not only interpretable image classification but also trustworthy recognition of OoD samples.

replacement¹ that is an indispensable step for grounding prototypes in the human-understandable space of training images [20]. Unfortunately, current methods either omit this replacement step [21], [22], [23], [24] for better task accuracy, but at the cost of compromising interpretability given that their prototypes are no longer represented by actual training image patches, or include the replacement step without addressing the performance degradation issue [10], [15], [18], [25]. Additionally, despite producing encouraging interpretable results, these discriminative classifiers miss an important explainability feature [26], [27], the recognition of Out-of-Distribution (OoD) inputs. Ideally, an XAI system should be able to explain its predictions regarding In-Distribution (ID) samples (interpretable) and meanwhile identify anomalous OoD samples to abstain from classifying them to ensure the decision trustworthiness. Furthermore, the prototype learning in current methods is an aggressive² approach that considers only the most salient object parts, disregarding important information available from less-salient object regions which could be helpful in the encoding of more difficult-to-learn visual features that have the potential to achieve improved classification.

Some issues mentioned above can be solved by generative models [19] to learn prototype distributions with the class-conditional data density $p(\mathbf{x}|c)$, where the classification decision is made according to Bayes' theorem. Through the explicitly modelling of data densities, generative models are particularly suitable for detecting OoD samples, as evidenced by numerous studies [19], [27], [28]. By revisiting the existing prototype-based networks, we showcase that with proper modifications, the prototypes from current point-based learning techniques can be represented by generative Gaussian mixture models (GMM), yielding our **Mixture of Gaussian-distributed Prototypes** (MGProto), as shown in Fig. 1(b), where each prototype is characterised by a rich GMM representation. A particularly beneficial implication

1. In the literature, the prototype replacement is also referred to as prototype “pushing” or “projection”. In this paper, we will use the terms replacement and projection interchangeably.

2. “Aggressive” refers to the fact that the prototype’s training process relies exclusively on the most salient object regions.

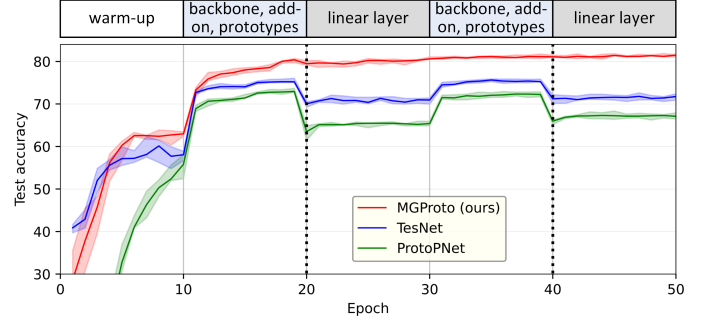


Fig. 2. Current prototype-based methods (e.g., ProtoPNet [10] and TesNet [15]) suffer from drastic performance degradation following the prototype replacement step (denoted by the dotted vertical lines) at each round of the multi-stage training, whereas our MGProto method does not encounter this problem. These curves are obtained from models trained on CUB-200-2011 using a ResNet34 backbone.

of this new type of prototype representation is its effectiveness in detecting OoD samples. Interestingly, the learning of our GMM-based prototypes has a natural prototype projection step, which effectively addresses the performance degradation issue, as shown in Fig. 2. Furthermore, instead of considering only the most salient object parts in the prototype learning, we present an effective method to further mine prototypes from sub-salient object regions, by drawing inspiration from a strategic approach that counters the winning strategy depicted in the classic Tian Ji’s horse-racing legend [29]. To allow model compactness, we propose pruning our MGProto model by discarding Gaussian-distributed prototypes with low importance. To summarise, our major contributions are:

- 1) We propose a new generative modelling of prototype distributions based on Gaussian mixture models, allowing both interpretable image classification and trustworthy recognition of OoD inputs.
- 2) We leverage MGProto’s optimisation to seamlessly project the learned prototype distributions back into the training sample space, thereby mitigating the performance drop caused by prototype projection.
- 3) We present a novel and generic approach to enhance prototype learning by mining prototypes from abundant less-salient object regions, inspired by the classic legend of Tian Ji’s horse-racing.
- 4) We introduce a method to compress our MGProto by adaptively pruning prototypical Gaussian components that hold low prototype importance.

Experimental results on CUB-200-2011, Stanford Cars, Stanford Dogs, and Oxford-IIIT Pets show that our proposed MGProto outperforms current state-of-the-art (SOTA) methods in terms of both image recognition and OoD detection. Moreover, our MGProto also exhibits promising quantitative interpretability results.

2 RELATED WORK

2.1 Interpretability with Prototypes

Efforts to understand deep learning networks often face challenges if relying solely on post-hoc techniques like saliency maps [30], [31], [32], [33], explanation surrogates [34], [35], [36], and counterfactual examples [37], [38],

[39]. These strategies fall short in explaining the network’s reasoning process, yielding results that may be unreliable and risky [3].

On the other hand, prototype-based networks provide an appealing way to access the model’s inner workings. These networks dissect a test image sample by finding prototypes and combining evidence from these prototypes to make a decision. ProtoPNet [10] is the original work that adopts a number of class-specific prototypes for interpretable image recognition. Built upon it, TesNet [15] introduces the orthonormal transparent basis concepts, and Deformable ProtoPNet [25] makes prototypes spatially-deformable to handle object variations. Other efforts extend prototypes to visual transformers [22], [24], K-nearest neighbour [40], knowledge distillation [41], and ensemble interpretations [18]. To gauge the prototype-based interpretability, two objective metrics are proposed, i.e., consistency and stability scores [21]. Also, some studies relax the class-specific constraint to allow a reduced number of prototypes [16], [24], [42], [43]. Recent works focus on refining semantically confounded or ambiguous prototypes [44], [45] in ProtoPNet. Promisingly, the prototype-based interpretable networks are being applied in critical tasks beyond the ones in computer vision [46], [47], [48], [49], [50].

The existing models above are trained with point-based learning techniques, yielding prototypes with limited representation power. As described in Section 1, the training for these prototypes involves a prototype projection into the training image space that causes drastic performance drop. Furthermore, it is challenging to recognise OoD inputs using these prototypes trained with point-based learning methods, thereby reducing the decision trustworthiness of the model. Even though PIP-Net [17], trained with point-based learning techniques, attempts to detect OoD samples, its detection performance is still far from satisfactory.

2.2 Gaussian Mixture Model

Gaussian Mixture Model (GMM) [51] is a probabilistic approach to represent data distributions with a mixture of Gaussian components, which has been extensively explored in a variety of applications, such as semantic segmentation [52], [53], point cloud registration [54], and image compression [55]. Recently, GMM has been used to explain inter-layer deep-learning features [56] with an approach designed to produce post-hoc explanations that fall short in explaining the network’s reasoning, which notably differs from our grey-box model with prototype-based interpretability. In this paper, we demonstrate that previous point-based prototype learning methods in the ProtoPNet family can be formulated with GMMs to explicitly capture the underlying class-conditional data distributions.

For estimating the parameters of GMM, the Expectation–Maximisation (EM) algorithm [57] is typically utilised, involving iterative steps of evaluating the data responsibility using the current parameters (E-step) and maximising the data log-likelihood (M-step). An advantage of our approach is that the M-step of GMM training relies on estimating the mean components of the Gaussian distributions with a weighted average of training samples, which naturally mitigates the performance degradation caused by the

projection of point-based learned prototypes. Also, while offering closed-form solutions, the standard EM algorithm often fails to ensure diverse Gaussian components, which results in potential prototype redundancy. We address this by incorporating a new constraint into the objective function of the M-step to encourage diversity of prototypes.

2.3 Tian Ji’s Horse Racing Legend

Tian Ji’s horse racing [29] is a well-known Chinese legend taking place between two parties of horse-racing enthusiasts: the general Tian Ji and the King Wei of Qi. Each party has three available horses, categorised into three speed levels: fast, regular, and slow. At the same speed level, the King’s horses are slightly faster than those of Tian. However, Tian’s horse in a superior level is able to beat King’s horse in an inferior level. They decide to hold a race with a total of three rounds, where in each round, both parties need to use a different horse. The party who wins the majority of the rounds wins the race. Initially, the King seems poised to win the race due to the faster speed of his horses at every level. However, Sun Bin, one of the most renowned military strategists in ancient Chinese history, proposes Tian a winning strategy: in the first round, Tian’s fast horse races against the King’s regular horse; in the second round, Tian’s regular horse races against the King’s slow horse; and in the third round, Tian’s slow horse races against the King’s fast horse. In such a strategy, Tian will win the race by winning two rounds while losing only one, as shown in Fig. 5(b).

The mathematical principle of this victorious strategy achieved more than 2000 years ago is still studied in modern game theory [58], [59]. In this work, we take inspiration from this legend to build an infallible winning strategy for the King: if the regular and the slow horses of the King are trained to be faster than the Tian Ji’s fast horse, then the King will always win the race by winning at each round. This infallible winning strategy of the King resembles our mining of prototypes from sub-salient object parts, elaborated in Section 3.4. To the best of our knowledge, we are the first to employ the horse-racing strategy in XAI research.

3 OUR MGPROTO METHOD

This section starts with a brief description of the current ProtoPNet-based networks with point-based learning of prototypes in Section 3.1, serving as preliminaries for our proposed MGProto method illustrated in Fig. 4. Then, we detail our MGProto that represents prototypes with Gaussian mixture models (Section 3.2), which are learned via a modified EM algorithm to ensure prototype diversity (Section 3.3). Additionally, we present a novel and generic approach to mine prototypes from sub-salient object regions to improve classification, as elaborated in Section 3.4.

3.1 Preliminaries

To better introduce our distribution-based prototypes, we first briefly revisit the current point-based prototype learning methods, e.g., ProtoPNet [10]. Let $\mathbf{x} \in \mathcal{X} \subset \mathbb{R}^{H \times W \times R}$ denote an image with size $H \times W$ and R colour channels, and $\mathbf{y} \in \mathcal{Y} \subset \{0, 1\}^C$ denote the one-hot image-level class

label with $\mathbf{y}_c = 1$ if the image class is c and $\mathbf{y}_c = 0$ otherwise. ProtoPNet includes the following four steps:

1) **The embedding step** feeds an image \mathbf{x} to a feature backbone $f_{\theta_{\text{bcb}}} : \mathcal{X} \rightarrow \mathcal{Z}$, parameterised by θ_{bcb} , to extract initial features $\mathbf{z} \in \mathcal{Z} \subset \mathbb{R}^{\bar{H} \times \bar{W} \times \bar{D}}$, which is passed on to several add-on layers $f_{\theta_{\text{add}}} : \mathcal{Z} \rightarrow \mathcal{F}$, parameterised by θ_{add} , to obtain feature maps $\mathbf{F} \in \mathcal{F} \subset \mathbb{R}^{\bar{H} \times \bar{W} \times D}$, where $\bar{H} \leq H$, $\bar{W} \leq W$ and D denotes the number of feature channels.

2) **The prototype-activating step** uses a set of learnable prototypes $\mathcal{P} = \{\mathbf{p}_m\}_{m=1}^{M \times C}$ to represent prototypical object parts (e.g., tails and beaks from class “bird”) in training images, where each of C classes has M prototypes and $\mathbf{p}_m \in \mathbb{R}^{1 \times 1 \times D}$. This step computes $M \times C$ similarity maps between the feature map \mathbf{F} and prototypes \mathcal{P} , which are formulated as $\mathbf{S}_m^{(i,j)} = \text{sim}(\mathbf{F}^{(i,j)}, \mathbf{p}_m)$, where $i \in \{1, \dots, \bar{H}\}$, $j \in \{1, \dots, \bar{W}\}$, $\mathbf{F}^{(i,j)} \in \mathbb{R}^{1 \times 1 \times D}$, and $\text{sim}(\cdot, \cdot)$ is a similarity metric (e.g., cosine similarity [25]). These similarity maps are then transformed into $M \times C$ similarity/activation scores from the max-pooling: $\mathbf{s}_m(\mathbf{x}) = \max_{i,j} \mathbf{S}_m^{(i,j)}$, where $m \in \{1, \dots, M \times C\}$.

3) **The aggregating step** computes the logit of class c by accumulating the similarity scores $\mathbf{s}_m(\mathbf{x})$ via a dense linear layer as in Fig. 1(a): $\text{logit}^c = \sum_{m=1}^{M \times C} \pi_m^c \mathbf{s}_m(\mathbf{x})$, where $\pi^c \in \mathbb{R}^{M \times C \times 1}$ is the layer’s connection weight with class $c \in \{1, \dots, C\}$. A softmax function is applied to the output logits of all classes to predict the posterior class probability $p(c|\mathbf{x}; \theta_{\text{bcb}}, \theta_{\text{add}}, \mathcal{P}, \pi)$, where $\theta_{\text{bcb}}, \theta_{\text{add}}, \mathcal{P}$ and π are parameters of ProtoPNet. Current ProtoPNet-based networks are optimised with point-based learning techniques to minimise the cross-entropy error between the posterior class probability and ground-truth image label.

4) **The replacement step** grounds prototypes in the image space, so that prototypes are exactly represented by the actual training image patches [20]. This is reached by replacing each prototype with the latent feature of its nearest image patch of the same class in the training set [10], [18], [25]. Mathematically, for a prototype \mathbf{p}_m of class c , we have:

$$\mathbf{p}_m \leftarrow \arg \max_{\mathbf{f} \in \mathbf{F}_{a \in \{1, \dots, |\mathcal{D}_c|\}}}} \text{sim}(\mathbf{f}, \mathbf{p}_m), \quad (1)$$

where \mathcal{D}_c is the set of training images from class c and \mathbf{f} is a latent feature vector of images in \mathcal{D}_c . Because the prototypes \mathcal{P} are updated over training mini-batches, it is impractical to conduct the replacement step too often during training, given that it requires to search the most similar patch in the training set for each prototype. Usually, this step occurs every several training epochs, as shown in Fig. 2, and it causes drastic performance drops for ProtoPNet and TesNet. To help understand this issue, Fig. 3 provides the T-SNE results of ProtoPNet and TesNet before the replacement, where we notice large distances or discrepancies between the point-based learned prototypes and their nearest training patch features. Such large distances explain why the sequential replacement causes drastic performance drops. A similar observation about this discrepancy can be found in [12].

ProtoPNet and its variants [15], [18], [25], [43] employ an iterative multi-stage optimisation scheme (see Fig. 2) that alternates between: 1) training model backbone, add-on layers, and prototypes; 2) prototype replacement; and 3) training of the linear aggregating layer. After sufficient

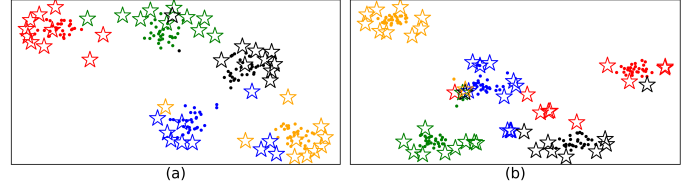


Fig. 3. T-SNE representations of prototypes (stars) and the nearest training patch features (dots), from ProtoPNet (a) and TesNet (b), trained on CUB-200-2011. We show 5 random classes (out of 200) for better visualisation, where each colour denotes a different class.

rounds, the performance degradation could be slightly alleviated, yet the final performance remains significantly deteriorated compared to the initial one.

3.2 Mixture of Gaussian-distributed Prototypes

According to Section 3.1, current discriminative networks rely on point-based learned prototypes \mathcal{P} that are used to compute similarity maps with \mathbf{F} . Instead, we leverage a Gaussian distribution to model our distribution-based prototypes and obtain likelihood maps whose value at the spatial position (i, j) denotes the confidence that the image patch fits the m -th prototype distribution of class c , as in:

$$\begin{aligned} \mathbf{H}_m^{(i,j),c} &= \mathcal{N}(\mathbf{F}^{(i,j)}; \mathbf{p}_m^c, \Sigma) \\ &= \frac{1}{(2\pi)^{\frac{D}{2}} |\Sigma|^{\frac{1}{2}}} e^{-\frac{1}{2} (\mathbf{F}^{(i,j)} - \mathbf{p}_m^c)^T \Sigma^{-1} (\mathbf{F}^{(i,j)} - \mathbf{p}_m^c)}, \end{aligned} \quad (2)$$

where the prototype $\mathbf{p}_m^c \in \mathbb{R}^D$ can be regarded as a mean of the Gaussian distribution, and $\Sigma \in \mathbb{R}^{D \times D}$ is a constant diagonal covariance matrix with diagonal value $1/2\pi$, so that the likelihood has a range in $[0, 1]$. Note that we treat the covariance as constant, so our Gaussian-distributed prototypes do not introduce any extra parameters compared to existing point-based learning methods. We also apply max-pooling on the likelihood maps to obtain class-wise maximum likelihood scores: $\mathbf{h}_m^c(\mathbf{x}) = \max_{i,j} \mathbf{H}_m^{(i,j),c}$, for $m \in \{1, \dots, M\}$ and $c \in \{1, \dots, C\}$.

In alignment with previous prototype-based networks [10], [18], [25] that employ a set of M prototypes to acquire a rich representation of a visual class, our MG-Proto also harnesses multiple prototype distributions for each class c , whose likelihood scores are accumulated by weighted sum in the aggregating layer, as shown in Fig. 1(b). This procedure naturally inspires us to derive the GMM formulation, which captures the class-conditional data density with a generative paradigm:

$$\begin{aligned} p(\mathbf{x}|c) &= \sum_{m=1}^M \pi_m^c \mathbf{h}_m^c(\mathbf{x}) = \sum_{m=1}^M \pi_m^c \max_{i,j} \mathbf{H}_m^{(i,j),c} \\ &= \sum_{m=1}^M \pi_m^c \max_{i,j} \mathcal{N}(\mathbf{F}^{(i,j)}; \mathbf{p}_m^c, \Sigma), \end{aligned} \quad (3)$$

where π_m^c is the mixture weights in GMMs to quantify prototype importance, which are referred to as *importance priors*. Also, π_m^c serves as the weights in the linear aggregating layer. From Eq. (3), the mixture model allows the prototype distributions of a class to collaboratively describe the underlying data density of that class. Meanwhile, these multiple

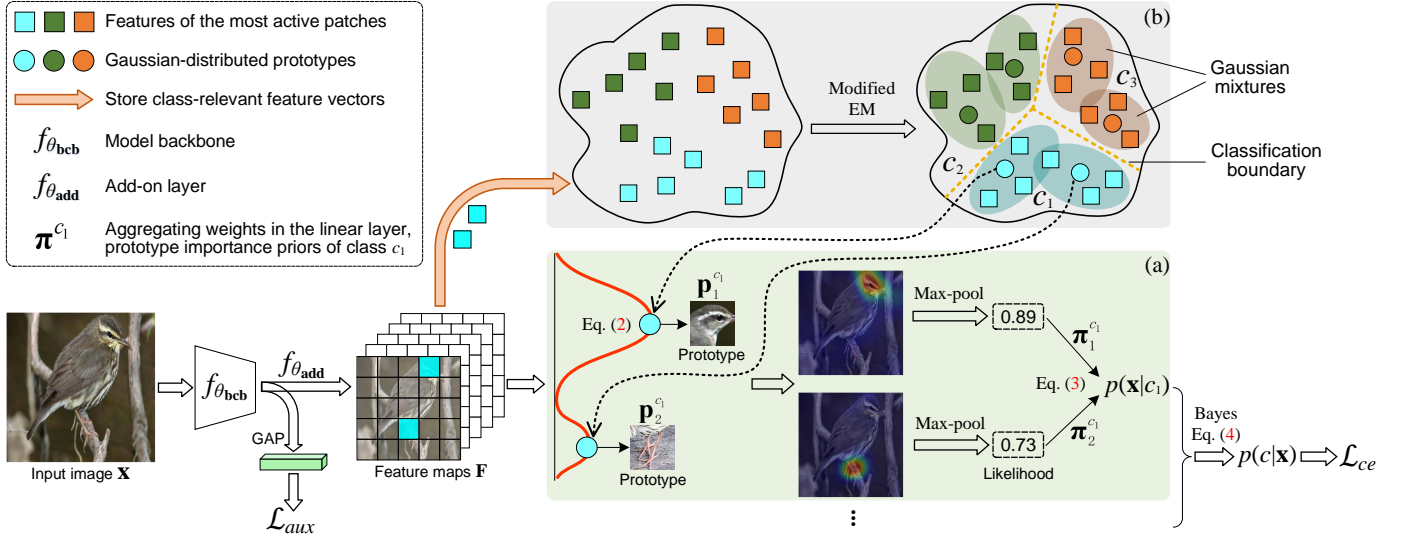


Fig. 4. The overall framework of the MGProto method. For a given image \mathbf{x} , the model backbone (e.g., ResNet) extracts initial features $f_{\theta_{bcb}}(\mathbf{x})$ that are then fed to the add-on layer $f_{\theta_{add}}$ to obtain feature maps \mathbf{F} . An auxiliary loss \mathcal{L}_{aux} is applied on $f_{\theta_{bcb}}(\mathbf{x})$ to improve the backbone's feature extraction ability. (a) The case-based interpretation is achieved by fitting the feature representation \mathbf{F} into the mixture of Gaussian-distributed prototypes, yielding the class-conditional data probability $p(\mathbf{x}|c)$ that enables the determination of whether the input is OoD. Bayes' theorem is then used to derive the posterior class probability $p(c|\mathbf{x})$ for predicting the image category and computing the cross-entropy loss \mathcal{L}_{ce} . For simplicity, here we show only 2 prototypes for class c_1 , thus only 2 relevant features from the most active image patches are stored to the memory queue of class c_1 . (b) For each class, the mixture of Gaussian-distributed prototypes is estimated by a modified EM algorithm to encourage prototype diversity.

prototype distributions in a mixture are enforced to compete against each other due to the inherent constraint in GMM: $\sum_{m=1}^M \pi_m^c = 1$ for each class c . Hence, we take advantage of this constraint to prune prototypes with low importance priors for promoting model compactness. It is worth noting that our MGProto utilises a concise aggregating layer (see Fig. 1(b)), represented by $\pi^c \in \mathbb{R}^{M \times 1}$, which differs from current methods [10], [18], [25] using a dense layer denoted by $\pi^c \in \mathbb{R}^{MC \times 1}$, as mentioned in Section 3.1. The use of our concise layer not only introduces prototype-class connection sparsity to reduce the explanation size [17], but also prevents the prediction of a class from being disturbed by prototypes of other classes [21].

Based on the well-known Bayes' theorem, the posterior class probability $p(c|\mathbf{x})$ is computed as

$$p(c|\mathbf{x}) = \frac{p(\mathbf{x}|c)p(c)}{\sum_{c'=1}^C p(\mathbf{x}|c')p(c')} = \frac{p(\mathbf{x}|c)}{\sum_{c'=1}^C p(\mathbf{x}|c')}, \quad (4)$$

by assuming $p(c) = \frac{1}{C}$ ³, as commonly adopted in the literature [61], [62], [63]. Relying on this assumption, the core of MGProto is to accurately estimate the class-conditional data density $p(\mathbf{x}|c)$ modelled with the mixture of Gaussian-distributed prototypes through Eq. (3).

Equipped with class-conditioned distributions, our MGProto can identify OoD inputs and abstain from classifying them to ensure decision trustworthiness. This is achieved by marginalising $p(\mathbf{x}|c)$ over all training classes to compute the overall data probability $p(\mathbf{x})$ that an input data belongs to

the distribution of the training set:

$$p(\mathbf{x}) = \sum_{c=1}^C p(\mathbf{x}|c)p(c) \propto \sum_{c=1}^C p(\mathbf{x}|c). \quad (5)$$

Based on Eq. (5), OoD inputs will have a low value for $p(\mathbf{x})$, which in practice means that \mathbf{x} will be far from the prototypes of any of the classes and, consequently, will not fit well the prototype distributions of any class. Notice that Eq. (5) is an energy-like criteria, which has been adopted for OoD detection by discriminative classifiers [64], but not by generative models, as explored in our approach.

The well-known expectation-maximisation (EM) algorithm [57] can be employed to estimate the prototype means \mathbf{p}^c and importance priors π^c for each class c . Nevertheless, the standard EM algorithm does not guarantee diverse characteristics of the Gaussian-distributed prototypes, a crucial aspect for enhancing the interpretability of prototypical-part methods [15], [18], [25]. Therefore, in the next Section 3.3, we introduce a modified EM strategy to encourage diversity of the prototypes during their learning.

3.3 Learning of Gaussian-distributed Prototypes

Section 3.2 describes the prototype means \mathbf{p}^c and importance priors π^c as parameters of the class-wise GMMs, defined in Eq. (3). The accurate optimisation of GMM parameters typically depends on the whole training set [51]. However, modern deep-learning networks are often trained in a mini-batch fashion, where only a limited number of training data is provided. That can harm GMM's predicative performance. To leverage a large set of feature representations for the GMM optimisation, we adopt the memory bank [65] mechanism that has proven effective in maintaining contextual information [66].

The memory bank is defined as a class-wise queue $\mathcal{B}^c \in \mathbb{R}^{N \times D}$ that stores *class-relevant* features from previously-

3. The datasets used in our work have fairly balanced training samples across classes, making the prior $p(c)$ identical for all classes. For the imbalanced scenario, the prior can be estimated from the observed training data distribution. Alternatively, resampling strategies [60] can be used during training, properly ensuring an identical prior.

processed training samples during learning, where N is the memory capacity. As shown in Fig. 4, after a training image of class c is processed by backbone and add-on layers, we obtain feature maps \mathbf{F} consisting of $\bar{H} \times \bar{W}$ feature vectors. Since the training images usually contain background regions, not all these feature vectors are discriminative and relevant to the class c . We thus store only M relevant feature vectors from the most active image patches into the queue \mathcal{B}^c that correspond to the nearest feature vectors to the M prototypes of class c . In other words, these M feature vectors have the largest likelihood to the M prototype distributions. Note that the memory bank can be discarded after training, thus incurring no extra overhead for testing.

Relying on the memory bank, our Gaussian-distributed prototypes $\{\mathbf{p}_m^c, \pi_m^c\}_{m=1}^M$ can be estimated via a modified EM algorithm to accurately describe the underlying data densities. The E-step computes the responsibility that each feature $\mathbf{f}_n^c \in \mathcal{B}^c$, where $n \in \{1, \dots, N\}$, is generated by m -th Gaussian-distributed prototype of class c :

$$\gamma_{n,m}^c = \frac{\pi_m^c \mathcal{N}(\mathbf{f}_n^c; \mathbf{p}_m^c, \Sigma)}{\sum_{m=1}^M \pi_m^c \mathcal{N}(\mathbf{f}_n^c; \mathbf{p}_m^c, \Sigma)}. \quad (6)$$

The standard EM algorithm provides a closed-form M-step solution [51] to estimate the prototype means:

$$\mathbf{p}_m^{c*} = \frac{1}{N_m} \sum_{n=1}^N \gamma_{n,m}^c \mathbf{f}_n^c, \text{ where } N_m = \sum_{n=1}^N \gamma_{n,m}^c. \quad (7)$$

However, the closed-form solution above does not guarantee the learning of diverse prototypes, which results in prototype redundancy and decreased performance in our experiments. Motivated by [67], we modify the M-step by explicitly incorporating a prototype diversity constraint, with:

$$\begin{aligned} \{\mathbf{p}_m^{c*}\}_{m=1}^M = \\ \arg \max_{\{\mathbf{p}_m^c\}_{m=1}^M} \frac{1}{N} \sum_{n=1}^N \sum_{m=1}^M \gamma_{n,m}^c \log(\pi_m^c \mathcal{N}(\mathbf{f}_n^c; \mathbf{p}_m^c, \Sigma)) \\ - \frac{1}{M(M-1)} \sum_{m_1=1}^M \sum_{m_2 \neq m_1}^M e^{-\|\mathbf{p}_{m_1}^c - \mathbf{p}_{m_2}^c\|^2}, \end{aligned} \quad (8)$$

where the first term aims to maximise the log-likelihood over all data in the memory bank \mathcal{B}^c and the second term improves prototype diversity by increasing within-class distances between prototype means. Note that Eq. (8) no longer has closed-form solution, so we update it using gradient descent. The update of the prototype importance priors π_m^c can still rely on the closed-form solution:

$$\pi_m^{c*} = \frac{1}{N} \sum_{n=1}^N \gamma_{n,m}^c. \quad (9)$$

The GMM optimisation involves iterative loops between the E-step and M-step. Since our memory bank evolves progressively during training, only few loops (denoted by L_{em}) are sufficient for good EM convergence.

According to Eq. (7) and Eq. (8), our MGProto has a natural prototype projection step, happening during the M-step with the estimation of the prototype means as the weighted average of nearest training features stored in the

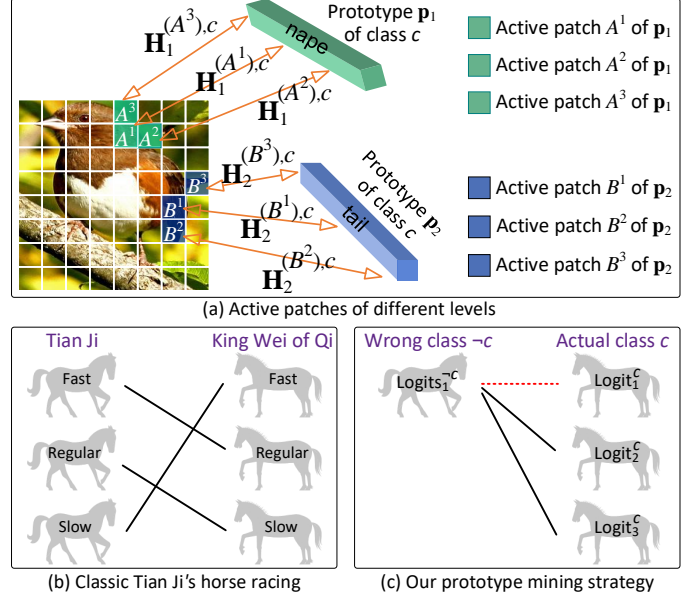


Fig. 5. (a) Illustration of different levels of active patches for prototype mining. For clarity, here we suppose only two prototypes in each class and consider $T = 3$ levels of active patches. (b) Diagram of the classic Tian Ji's horse racing legend. (c) Our proposed prototype mining strategy establishes $T - 1$ mining competitions (solid lines). The standard classification supervision is represented by the dash line.

memory queue, where the weight is the responsibility in Eq. (6) that is determined by the relative affinity to the currently-estimated prototypes. Obviously, similar features to the prototypes will have larger weights and dominate the soft assignment process. By contrast, the prototype replacement in Eq. (1) of existing methods are hard assignment of feature points, usually causing drastic performance drops.

3.4 Mining of Prototypes from Sub-salient Object Parts

Similar to many existing methods that utilise a max-pooling operation in Eq. (3) to select the positions with the highest likelihood score, so far our prototype learning process aggressively harnesses only the most active patches (i.e., object parts) in an image. This means that during training, the learning process never involves the remaining less-active patches. As a result, the prototypes will focus on only the most salient or discriminative object parts and overlook crucial information from other sub-salient object regions. Intuitively, these sub-salient regions encapsulate rich difficult-to-learn visual patterns that can be exploited to achieve improved classification. In Fig. 5(a), we illustrate different levels of the active patches which have different likelihood scores for the same prototype.

In this paper, we present a novel and generic strategy, inspired by the ancient Tian Ji's horse racing legend [29], to mine prototypes from sub-salient object regions. As illustrated in Fig. 5(b), the essence of this legend is that the ranking order of Tian's horses should be wisely shifted, to allow Tian to win two out of the three rounds. We instead propose an infallible winning strategy for the King, consisting of training the King's regular and slow horses to be faster than Tian's fast horse.

We elaborate below how to formulate the new prototype mining strategy. Assume that we have a training image \mathbf{x}

labelled with class c . We consider T sequential patch levels from the most to the least active, such as $\{A^1, A^2, \dots, A^T\}$ of the prototype \mathbf{p}_1 and $\{B^1, B^2, \dots, B^T\}$ of the prototype \mathbf{p}_2 , as in Fig. 5(a). According to Eq. (3), the predicted logit⁴ for each patch level $t \in \{1, \dots, T\}$ is computed as the weighted sum of likelihood scores $p(\mathbf{x}|c)$: $\text{logit}_t^c = \pi_1^c \times \mathbf{H}_1^{(A^t),c} + \pi_2^c \times \mathbf{H}_1^{(B^t),c}$. Obviously, we have $\text{logit}_T^c < \text{logit}_{T-1}^c < \dots < \text{logit}_1^c$ because $\mathbf{H}_1^{(A^T),c} < \mathbf{H}_1^{(A^{T-1}),c} < \dots < \mathbf{H}_1^{(A^1),c}$ and $\mathbf{H}_1^{(B^T),c} < \mathbf{H}_1^{(B^{T-1}),c} < \dots < \mathbf{H}_1^{(B^1),c}$. We showcase our prototype mining strategy in Fig. 5(c), which is analogous to the legend. To propose the infallible winning strategy for the King, we regard: 1) the most active logit of the wrong classes $\neg c$, denoted by $\text{logits}_1^{\neg c} \in \mathbb{R}^{C-1}$, as Tian Ji's fast horse; and 2) the $T-1$ less active logits of the actual class c , denoted by $\text{logit}_{t \in \{2, \dots, T\}}^c$, as the King's horses, except for the most active one denoted by logit_1^c . Then, we devise $T-1$ mining competitions: $\text{logits}_1^{\neg c}$ vs. $\text{logit}_{t \in \{2, \dots, T\}}^c$, which are supervised by the following mining loss with the goal of increasing $\text{logit}_{t \in \{2, \dots, T\}}^c$:

$$\mathcal{L}_{mn}(\mathbf{x}, \mathbf{y}) = \frac{1}{T-1} \sum_{t=2}^T \mathcal{L}_{ce}([\text{logits}_1^{\neg c}, \text{logit}_t^c], \mathbf{y}), \quad (10)$$

where $\mathcal{L}_{ce}(\cdot)$ is the cross-entropy (CE) loss and \mathbf{y} is the ground-truth label of \mathbf{x} . Here we employ $[\text{logits}_1^{\neg c}, \text{logit}_t^c] \in \mathbb{R}^C$ to represent the combined mining logits corresponding to the solid lines in Fig. 5(c), with $[\text{logits}_1^{\neg c}, \text{logit}_1^c] \in \mathbb{R}^C$ denoting the standard classification logits, shown as the dash line, which is supervised by:

$$\mathcal{L}_{ce}(\mathbf{x}, \mathbf{y}) = \mathcal{L}_{ce}([\text{logits}_1^{\neg c}, \text{logit}_1^c], \mathbf{y}), \quad (11)$$

Different from the legend in Fig. 5(b), our prototype mining leverages all $\text{logit}_{t \in \{2, \dots, T\}}^c$ with $T-1$ patch levels as in Eq. (10) to compete with the unique and most active $\text{logits}_1^{\neg c}$ to ensure an infallible winning strategy for the King, which also yields a stronger mining effect. To sum up, the major connections between our prototype mining and the classic horse-racing legend are: Tian Ji achieves victory through clever tactics in the legend. In contrast, our prototype mining approach devises a guaranteed winning strategy for the King, by training the King's regular and slower horses to ensure they surpass Tian Ji's fastest horse. Our proposed prototype mining strategy can be readily applied to a wide range of prototypical-part networks, for improved classification.

3.5 Training Objective and Prototype Replacement

The overall training objective of our proposed MGProto method for a mini-batch \mathcal{K} is defined as:

$$\mathcal{L}_{total} = \frac{1}{|\mathcal{K}|} \sum_{(\mathbf{x}, \mathbf{y}) \in \mathcal{K}} \mathcal{L}_{ce}(\mathbf{x}, \mathbf{y}) + \lambda_1 \mathcal{L}_{mn}(\mathbf{x}, \mathbf{y}) + \lambda_2 \mathcal{L}_{aux}(\mathbf{x}, \mathbf{y}), \quad (12)$$

where λ_1 and λ_2 are hyper-parameters. In Eq. (12), the Proxy-Anchor [68] auxiliary loss $\mathcal{L}_{aux}(\cdot)$, proposed in the field of deep metric learning, is used to enhance the features

4. In our generative MGProto, the class-conditional data probability $p(\mathbf{x}|c)$ serves as the model's prediction logits, but we still use the symbol **logit** here, given the generality of the proposed mining strategy to the existing discriminative-based prototypical-part networks.

Algorithm 1: Training Procedure of MGProto

Data: Training set \mathcal{D} , Training epochs E .

Result: Model backbone θ_{bcb} and add-on layer θ_{add} ,
Prototypes $\{\mathbf{p}_m^c, \pi_m^c\}_{m=1}^M$ for $c \in \{1, \dots, C\}$.

```

/* Alternate Training */
1 for  $E$  Epochs do
2   Given a mini-batch  $\mathcal{K}$  sampled from  $\mathcal{D}$ ;
3   Compute loss  $\mathcal{L}_{total}$  in Eq. (12);
4   Update backbone  $\theta_{\text{bcb}}$  and add-on layer  $\theta_{\text{add}}$ ;
5   Update memory queue  $\mathcal{B}^c$  for each class  $c$ ;
6   for  $L_{em}$  Loops do
7     E-step: compute responsibility in Eq. (6);
8     M-step: update  $\mathbf{p}_m^c$  in Eq. (8) and
9           update  $\pi_m^c$  in Eq. (9);
/* Prototype Replacement */
10 Ground prototype means  $\mathbf{p}_m^c$  in Eq. (14);
/* Model Pruning (Optional) */
11 Keep prototypes with top- $\tilde{M}$  priors for each class  $c$ .
```

extracted by the model backbone, as suggested by [40]. Specifically, we employ a Global Average Pooling (GAP) operator to condense the initial deep features $\mathbf{z} = f_{\theta_{\text{bcb}}}(\mathbf{x})$ into the embedding vector $\mathbf{e} = \text{GAP}(\mathbf{z}) \in \mathbb{R}^{\tilde{D}}$, where the loss is computed with:

$$\mathcal{L}_{aux}(\mathbf{x}, \mathbf{y}) = \frac{1}{|\mathcal{Q}^+|} \sum_{\mathbf{q} \in \mathcal{Q}^+} \log \left(1 + \sum_{\mathbf{e} \in \mathcal{E}_{\mathbf{q}}^+} e^{-\alpha(\text{sim}(\mathbf{e}, \mathbf{q}) - \delta)} \right) + \frac{1}{|\mathcal{Q}^-|} \sum_{\mathbf{q} \in \mathcal{Q}^-} \log \left(1 + \sum_{\mathbf{e} \in \mathcal{E}_{\mathbf{q}}^-} e^{\alpha(\text{sim}(\mathbf{e}, \mathbf{q}) + \delta)} \right), \quad (13)$$

where $\mathcal{Q} = \{\mathbf{q}_1, \dots, \mathbf{q}_C\}$ denotes the set of learnable proxies for all classes (a proxy is a global representative class-wise anchor in the embedding space [68] and one proxy for each class), and $\mathcal{Q}^+ \subset \mathcal{Q}$ is the set of proxies for the classes present in the mini-batch \mathcal{K} . The set of embeddings \mathbf{e} of the samples, computed with $\text{GAP}(\cdot)$, from the mini-batch \mathcal{K} is divided into the sets $\mathcal{E}_{\mathbf{q}}^+$ and $\mathcal{E}_{\mathbf{q}}^-$ containing the batch of embeddings with the same class or different class as the proxy \mathbf{q} , respectively. In Eq. (13), the function $\text{sim}(\cdot, \cdot)$ computes the cosine similarity, δ and α are hyper-parameters ($\delta = 0.1$ and $\alpha = 32$, as in the original paper [68]).

As detailed in Algorithm 1, the main training procedure of MGProto alternates between two steps: 1) optimising the model backbone and add-on layer $\{\theta_{\text{bcb}}, \theta_{\text{add}}\}$ using Eq. (12), with the prototype distributions $\{\mathbf{p}_m^c, \pi_m^c\}$ frozen; and 2) estimating the prototype distributions via the modified EM algorithm through Eq. (6), (8), and (9), with the model backbone and add-on layers frozen. Note that an additional warm-up stage is needed to fill the memory queue \mathcal{B}^c with sufficient class-relevant features.

Although the optimisation of our MGProto includes a natural prototype replacement, we still need a way of visualising and grounding the prototypes in the image space, so that they are represented by actual training image patches. Similar to Eq. (1), we accomplish this by replacing each of the prototype means with the latent feature vector of its

most active training image patch from the same class, with:

$$\mathbf{p}_m^c \leftarrow \arg \max_{\mathbf{f} \in \mathbf{F}_{a \in \{1, \dots, |\mathcal{D}_c|\}}}} \mathbf{H}_m^c, \quad (14)$$

where \mathbf{H}_m^c is the likelihood map defined in Eq. (2). As shown in Fig. 2, our MGProto no longer suffers from performance degradation in the replacement step.

3.6 MGProto Pruning by Prototype Importance Prior

Pruning is a good way of reducing the explanation size of interpretable prototypical-part networks [69]. In practice, it is often implemented by discarding prototypes that are irrelevant, meaningless, or ambiguous [10], [16], [42], [44].

In this work, we propose to remove less-important or trivial prototypes in a trained MGProto model, resorting to the inherent mixture constraint of GMMs: $\sum_{m=1}^M \pi_m^c = 1$ for each class c , as mentioned in Section 3.2. To be specific, we take advantage of the prototype importance prior π_m^c , where a large (or low) prior means the respective prototype is important (or trivial) to characterise the underlying class-conditional distribution $p(\mathbf{x}|c)$. Based on the above analysis, we prune a trained MGProto by keeping only important prototypes corresponding to the top- \tilde{M} priors for each class, where $\tilde{M} < M$. This can avoid choosing complicated per-class pruning thresholds, which is required in previous pruning schemes [10], [16].

4 EXPERIMENTS

4.1 Datasets and Evaluation Metrics

We evaluate our method on three standard fine-grained image recognition benchmarks: CUB-200-2011 [70], Stanford Cars [71], and Stanford Dogs [72]. To follow the same setting of OoD detection in PIP-Net [17], we also use Oxford-IIIT Pets [73]. Images are resized to 224×224 and we apply the same online augmentations [16], [40] to training images.

Image recognition and OoD detection performances are evaluated using the top-1 accuracy and FPR95 metrics, respectively. Following [17], [18], [21], we quantify different facets of interpretability on CUB using full images, with: 1) *Consistency* score that quantifies how consistently each prototype activates the same human-annotated object part [21]; 2) *Purity* of prototypes which, similarly to the consistency score, evaluates the extent that the top-10 image patches for a prototype can encode the same object-part [17]; 3) *Stability* score that measures how robust the activation of object parts is when noise is added to an image input [21]; 4) *Outside-Inside Relevance Ratio* (OIRR) which calculates the ratio of mean activation outside the object to those within the object, using ground-truth object segmentation masks [74]; and 5) *Deletion AUC* (DAUC) that computes the degree in the probability drop of the predicted class as more and more activated pixels are erased [75]. The above consistency, purity, and stability are part-level measures, OIRR is an object-level measure, and DAUC is a model-level measure based on causality.

4.2 Implementation Details

We perform experiments on various CNN backbone architectures: VGG16 (V16), VGG19 (V19), ResNet34 (R34), ResNet50 (R50), ResNet152 (R152), DenseNet121 (D121), and DenseNet161 (D161), which are all pre-trained on ImageNet [76], except for ResNet50 on CUB that is pre-trained on iNaturalist [77]. In accordance with prior studies, the prototype dimension $D = 64$ and prototype number $M = 10$ for all backbones and datasets. Following [17], [25], we obtain more fine-grained feature maps with $\tilde{H} = \tilde{W} = 14$ by dropping the final max-pooling layer in the backbones. Then two add-on 1×1 convolutional layers (without activation function⁵) are appended to reduce the number of feature channels to match the prototype dimension, thereby improving the computational efficiency. The memory capacity N is set to 800, 1000, 2000, 2000 for CUB, Cars, Dogs, and Pets, respectively. In Eq. (12), we have $\lambda_1 = 0.2$, and λ_2 is set as 0.5 according to [40]. For the prototype mining, we use $T = 20$ levels of active patches.

Our MGProto is implemented with PyTorch [78] and trained with Adam optimiser, using a mini-batch size $|\mathcal{K}| = 80$. The learning rates for the CNN backbone are chosen as 1×10^{-4} (CUB, Cars, and Pets) and 1×10^{-5} (Dogs). The learning rates of add-on layers are set as 3×10^{-3} for all datasets. These learning rates are decreased by 0.4 every 15 epochs (with a total of $E = 120$ training epochs). For the optimisation of prototype means in Eq. (8), the learning rates of gradient descent are 3×10^{-3} (CUB) and 3×10^{-4} (Cars, Dogs, and Pets). We set the number of EM loops $L_{em} = 3$. To improve the EM solution, an exponential moving average (EMA) [79] is used in the M-step: $\{\pi_m^c\}_{ema}^{t+1} := \tau \{\pi_m^c\}_{ema}^t + (1 - \tau) \{\pi_m^c\}^t$, where $\tau = 0.99$. Also, we experimentally noticed that for a few classes, all feature samples in the memory queue tend to have a large responsibility for a single Gaussian prototype in the E-step, ignoring other prototypes. We alleviate this issue with an additive smoothing [80], [81] to soften the calculated responsibility in Eq. (6) for each feature sample: $\gamma_{n,m}^{c, \text{soft}} = (\gamma_{n,m}^c + \alpha) / (\sum_{m=1}^M (\gamma_{n,m}^c + \alpha))$, where $\alpha = 0.1$.

4.3 Comparison With SOTA Methods

4.3.1 Accuracy of Interpretable Image Recognition

Table 1 shows the comparison results with other SOTA ProtoPNet variants using full CUB images, where the Baseline denotes a non-interpretable black-box model. Across all CNN backbones, our MGProto consistently achieves the highest accuracy, when using 10 prototypes per class. Even when trained with fewer prototypes (2 per class, totalling 400), MGProto remains highly effective, outperforming other methods like ProtoPool and ProtoKNN by a significant margin. Table 2 shows the classification results on Cars. Following [10], [40], [43], we also crop Car images using the provided bounding boxes to perform experiments. As evident, our MGProto exhibits the best accuracy under both settings of full and cropped images. Table 3 further displays the superiority of MGProto on Stanford Dogs.

5. Two convolutional layers without a non-linear activation between them are functionally similar to applying a single convolutional layer. Here we choose the two-layer structure for consistency with many prior ProtoPNet-based methods.

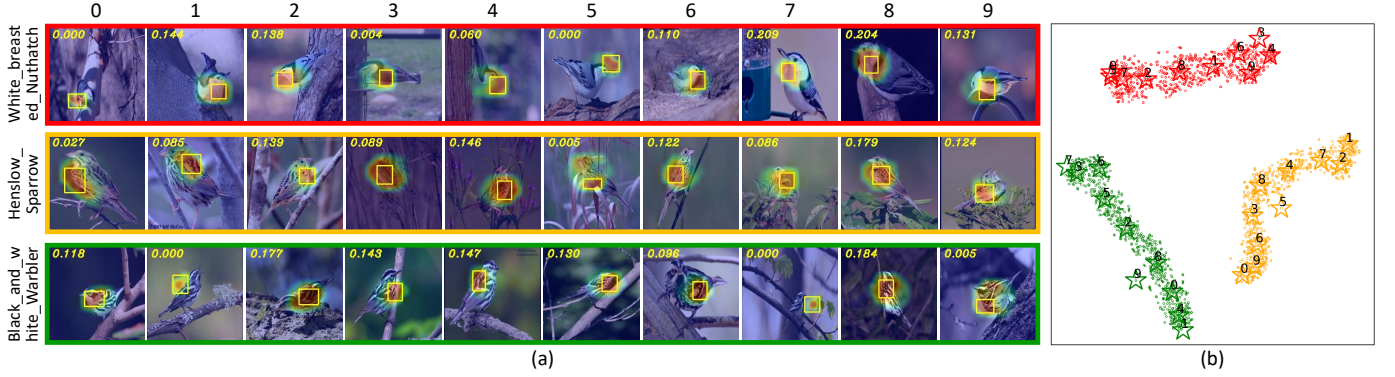


Fig. 6. Visual prototypes (a) and T-SNE results (b) from a ResNet34-based MGProto model, trained on CUB. These prototypes are marked with a yellow box in the activation maps, with the corresponding importance prior given in yellow text. In T-SNE, we show the prototypes (stars), their ID (numbers), and the nearest training features (dots) stored in the memory queue. This figure randomly shows 3 out of 200 classes, where each colour indicates a different class and for each class we display all 10 prototypes.

TABLE 1

Classification accuracy (%) on full images of CUB-200-2011, where 1×1p, 10pc denotes 1×1 prototype shape and 10 prototypes per class. We report our results as the mean and standard deviation over 5 runs.

| Method | # Proto. | V16 | V19 | R34 | R50 | R152 | D121 | D161 |
|--------------------|------------|-----------|-----------|-----------|-----------|-----------|-----------|-----------|
| Baseline | n.a. | 70.9 | 71.3 | 76.0 | 78.7 | 79.2 | 78.2 | 80.5 |
| ProtoPool [43] | 1×1p, 202 | 74.8 | 75.3 | 76.2 | 83.4 | 79.9 | 78.1 | 80.0 |
| ProtoKNN [40] | 1×1p, 512 | 77.2 | 77.6 | 77.6 | 87.0 | 80.6 | 79.8 | 81.4 |
| MGProto | 1×1p, 400 | 79.1(0.3) | 79.3(0.1) | 81.0(0.2) | 87.3(0.2) | 81.6(0.1) | 80.6(0.2) | 82.3(0.3) |
| ProtoPNet [10] | 1×1p, 10pc | 70.3 | 72.6 | 72.4 | 81.1 | 74.3 | 74.0 | 75.4 |
| ProtoConcepts [45] | 1×1p, 10pc | 70.6 | 72.7 | 73.0 | 81.7 | 74.7 | 73.8 | 75.7 |
| TesNet [15] | 1×1p, 10pc | 75.8 | 77.5 | 76.2 | 86.5 | 79.0 | 80.2 | 79.6 |
| Deformable [25] | 2×2p, 10pc | 75.7 | 76.0 | 76.8 | 86.4 | 79.6 | 79.0 | 81.2 |
| ST-ProtoPNet [18] | 1×1p, 10pc | 76.2 | 77.6 | 77.4 | 86.6 | 78.7 | 78.6 | 80.6 |
| SDFA-SA [21] | 1×1p, 10pc | 76.4 | 77.7 | 77.8 | 86.4 | 79.9 | 80.4 | 81.4 |
| MGProto | 1×1p, 10pc | 80.6(0.3) | 80.4(0.1) | 82.2(0.2) | 87.8(0.1) | 82.8(0.2) | 81.8(0.3) | 84.1(0.2) |

TABLE 2

Classification accuracy (%) on Stanford Cars based on ResNet50 backbone, trained and tested using "Crop" and "Full" car images. We report our results as the mean and standard deviation over 5 runs.

| Data | ProtoPNet [10] | ProtoTree [16] | ProtoPool [43] | PIP-Net [17] | ProtoKNN [40] | MGProto |
|------|----------------|----------------|----------------|--------------|---------------|-----------|
| Crop | 88.4 | 89.2 | 88.9 | 90.2 | 90.9 | 92.0(0.1) |
| Full | 86.1 | 86.6 | 86.3 | 86.5 | — | 89.2(0.2) |

Fig. 6 visualises all 10 prototypes for 3 classes from CUB, and T-SNE representations of prototypes and training features from our MGProto. It can be observed that: 1) large-prior prototypes, which dominate the decision making, are always from high-density distribution regions (in T-SNE) and can localise well the object (bird) parts; 2) background prototypes tend to have a low prior and come from the low-density distribution regions; 3) some prototypes localise the object parts but have a low prior, suggesting that those object parts may not be important for identifying that class; 4) the prototypes naturally localise at the centre of data clusters (in T-SNE), which prevents a decrease in performance when replacing prototypes with the nearest features.

TABLE 3

Classification accuracy (%) on full images of Stanford Dogs. We report our results as the mean and standard deviation over 5 runs.

| Method | # Proto. | V16 | V19 | R34 | R50 | R152 | D121 | D161 |
|--------------------|------------|-----------|-----------|-----------|-----------|-----------|-----------|-----------|
| Baseline | n.a. | 75.6 | 77.3 | 81.1 | 83.1 | 85.2 | 81.9 | 84.1 |
| ProtoPNet [10] | 1×1p, 10pc | 70.7 | 73.6 | 73.4 | 76.4 | 76.2 | 72.0 | 77.3 |
| ProtoConcepts [45] | 1×1p, 10pc | 71.2 | 73.8 | 73.7 | 76.2 | 76.9 | 72.5 | 77.5 |
| TesNet [15] | 1×1p, 10pc | 74.3 | 77.1 | 80.1 | 82.4 | 83.8 | 80.3 | 83.8 |
| Deformable [25] | 3×3p, 10pc | 75.8 | 77.9 | 80.6 | 82.2 | 86.5 | 80.7 | 83.7 |
| ST-ProtoPNet [18] | 1×1p, 10pc | 74.2 | 77.2 | 80.8 | 84.0 | 85.3 | 79.4 | 84.4 |
| SDFA-SA [21] | 1×1p, 10pc | 73.9 | 77.1 | 81.4 | 84.3 | 85.9 | 80.1 | 84.7 |
| MGProto | 1×1p, 10pc | 75.6(0.2) | 78.8(0.1) | 83.6(0.3) | 85.9(0.2) | 87.7(0.1) | 81.9(0.3) | 86.1(0.3) |

TABLE 4

FPR95 (%) of OoD detection for each ID-OoD pair, computing the false positive rate (FPR) of OoD samples when the true positive rate of ID samples is at 95%. The models are trained using only ID samples.

| Method | CUB-Cars | CUB-Pets | Cars-CUB | Cars-Pets | Pets-CUB | Pets-Cars |
|--------------|----------|----------|----------|-----------|----------|-----------|
| PIP-Net [17] | 1.1 | 8.1 | 7.8 | 5.6 | 12.9 | 0.9 |
| MGProto | 0.05 | 7.6 | 3.2 | 2.0 | 8.0 | 0.08 |

4.3.2 Accuracy of Trustworthy Image Recognition

Our MGProto is capable of identifying OoD inputs and abstaining from making decisions on them, thereby achieving trustworthy image recognition, through Eq. (5). Following PIP-Net [17], we use ResNet50 backbone and perform experiments on CUB, Cars, and Pets (e.g., choose one dataset as ID and the other two as OoD). Table 4 shows that MGProto outperforms PIP-Net by a large margin in most tasks. For example, when trained on Cars and classifying 95% of the testing Cars images as ID samples, MGProto detects 96.8% of CUB images as OoD, while PIP-Net only detects 92.2% under the same setting. Fig. 7 depicts the probability histogram for the task of CUB as ID, Cars and Pets as OoD, revealing that our MGProto produces high probability for ID samples and low probability for OoD samples. Fig. 7 also suggests that CUB images have smaller semantic distance to Pets than Cars, which is aligned with our human intuition.

Fig. 8(a) displays an example of the interpretable and trustworthy reasoning of our MGProto for classifying an ID sample (Le Conte Sparrow image from CUB test set). In this case, the model obtains the highest $p(x|c)$ for the class Le Conte Sparrow among all classes, meaning that the input image data fits best the prototype distributions of this class. Hence, our model classifies the image as Le Conte Sparrow. Additionally, our method evaluates the overall data probability $p(x)$ that the input data belongs to the distribution of the training set. Here, the $p(x) \propto 2.429$, surpassing the OoD detection threshold in Fig. 7, our model thus treats the input image as an ID sample, which means that the classification decision is trustworthy and should be accepted. Fig. 8(b) shows an example of our MGProto method recognising an OoD sample (Keeshond image from Pets), where the input image obtains $p(x)$ smaller than the OoD detection threshold. The model opts to abstain from classifying the image since it does not fit well the CUB-prototype distributions of all 200 classes.

TABLE 5

Comparison with specialised OoD detection approaches, evaluated with FPR95 (%) and AUROC (%). We show the results on each individual OoD dataset and the results on average across all five OoD datasets.

| Method | OoD Dataset | | | | | | | | | | | |
|------------------|-------------|--------------|--------------|--------------|-------------|--------------|-------------|--------------|--------------|--------------|--------------|--------------|
| | SVHN | | Places365 | | LSUN | | iSUN | | Textures | | Average | |
| | FPR95↓ | AUROC↑ | FPR95↓ | AUROC↑ | FPR95↓ | AUROC↑ | FPR95↓ | AUROC↑ | FPR95↓ | AUROC↑ | FPR95↓ | AUROC↑ |
| MSP [96] | 59.66 | 91.25 | 62.46 | 88.64 | 51.93 | 92.73 | 54.57 | 92.12 | 66.45 | 88.50 | 59.01 | 90.65 |
| ODIN [97] | 20.93 | 95.55 | 63.04 | 86.57 | 31.92 | 94.82 | 33.17 | 94.65 | 56.40 | 86.21 | 41.09 | 91.56 |
| Energy [64] | 54.41 | 91.22 | 42.77 | 91.02 | 23.45 | 96.14 | 27.52 | 95.59 | 55.23 | 89.37 | 40.68 | 92.67 |
| Mahalanobis [83] | 9.24 | 97.80 | 83.50 | 69.56 | 67.73 | 73.61 | 6.02 | 98.63 | 23.21 | 92.91 | 37.94 | 86.50 |
| ViM [98] | 24.95 | 95.36 | 63.04 | 86.57 | 7.26 | 98.53 | 33.17 | 94.65 | 56.40 | 86.21 | 36.96 | 92.26 |
| ReAct [99] | 48.16 | 92.32 | 37.25 | 93.13 | 18.09 | 96.91 | 20.35 | 95.59 | 96.51 | 47.41 | 34.25 | 94.09 |
| KNN [84] | 24.53 | 95.96 | 50.90 | 89.14 | 25.29 | 95.69 | 25.55 | 95.26 | 27.57 | 94.71 | 30.77 | 94.15 |
| ConjNorm [86] | 18.71 | 96.48 | 53.44 | 89.18 | 22.20 | 95.95 | 22.64 | 95.87 | 25.80 | 95.11 | 28.56 | 94.52 |
| ASH [100] | 28.94 | 94.84 | 27.29 | 91.31 | 9.06 | 98.34 | 21.61 | 95.95 | 35.02 | 93.63 | 27.29 | 94.81 |
| GEM [85] | 37.41 | 93.22 | 38.40 | 91.50 | 10.81 | 97.90 | 12.36 | 97.57 | 28.88 | 94.38 | 25.57 | 94.91 |
| GEN [101] | 26.10 | 93.83 | 37.40 | 93.42 | 8.99 | 98.39 | 24.09 | 95.03 | 26.62 | 94.13 | 24.64 | 94.96 |
| NCA [89] | 14.33 | 96.05 | 26.73 | 91.85 | 19.28 | 96.83 | 29.88 | 94.86 | 17.03 | 95.64 | 21.45 | 95.05 |
| MGProto | 28.56 | 94.38 | 39.40 | 91.38 | 10.74 | 98.03 | 28.20 | 94.75 | 12.26 | 97.59 | 23.83 | 95.23 |

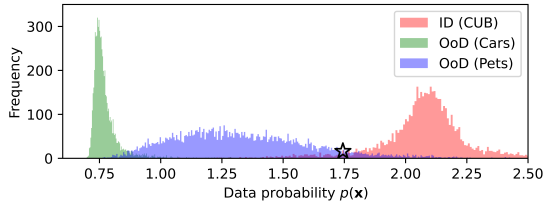


Fig. 7. Histograms of the overall data probability $p(x)$ computed on ID's test set and OoD's datasets. MGProto abstains from making a decision on an input x if $p(x)$ falls below a threshold marked by the star.

Notice that the OoD detection is a long-standing research topic, and mainstream approaches harness post-hoc analysis, which builds a scoring criterion (e.g., logit-based [64], [82], distance-based [83], [84], and density-based [85], [86]) to indicate the ID-ness of the input. Relying on these scores, subsequent studies boost the OoD detection with auxiliary training data from outlier exposure [87] or synthesis [88]. To explore where the ProtoPNet-based methods stand in comparison with specialised OoD detection approaches, we also experiment on the standard CIFAR-10 benchmark. Consistent with the setup in [84], [89], we utilise CIFAR-10 [90] as ID dataset and the same model backbone (ResNet-18) in our method. OoD datasets include: SVHN [91], Places365 [92], LSUN [93], iSUN [94], and Textures [95]. In line with prior post-hoc approaches, we employ only ID data for model's training, without using any auxiliary OoD training data. Experimental results in Table 5 demonstrate that our distribution-based prototypes achieve the best results on Textures dataset and deliver comparable average performances on par with other leading OoD detection approaches. In particular, our MGProto method greatly outperforms GEM [85] that models the class-conditional density using only a single Gaussian distribution, since our method leverages mixture of Gaussian distributions, enabling a more accurate characterization of the true underlying data density for each class.

4.3.3 Pruning of MGProto Model

Table 6 shows the MGProto pruning results. We first attempt to apply the purity-based pruning strategy [10] to our MGProto, but only a few prototypes are removed. This means that the strategy is improper to our method, mostly because our prototypes have large purity, evidenced in Table 8. On the other hand, if the merge-based pruning [42] is adopted,

TABLE 6

Model pruning results of our MGProto on CUB-200-2011, using different pruning strategies. % Pruned denotes the ratio between the number of pruned prototypes to that of the initial ones.

| Pruning strategy | # Initial Proto. | ResNet34 | | | ResNet152 | | |
|-------------------------|------------------|----------|----------|-------------|-----------|----------|-------------|
| | | # Proto. | % Pruned | Acc. (%) | # Proto. | % Pruned | Acc. (%) |
| Purity-based [10] | 2000 | 1993 | 0.35 | 82.2 → 82.2 | 1987 | 0.65 | 82.8 → 82.8 |
| Merge-based [42] | 2000 | 583 | 70.9 | 82.2 → 78.8 | 982 | 50.9 | 82.8 → 73.0 |
| Importance-based (ours) | 2000 | 1600 | 20.0 | 82.2 → 82.4 | 1600 | 20.0 | 82.8 → 82.9 |
| | 2000 | 1200 | 40.0 | 82.2 → 82.0 | 1200 | 40.0 | 82.8 → 82.4 |
| | 2000 | 800 | 60.0 | 82.2 → 81.8 | 800 | 60.0 | 82.8 → 82.0 |
| | 2000 | 400 | 80.0 | 82.2 → 81.1 | 400 | 80.0 | 82.8 → 81.3 |
| | 2000 | 200 | 90.0 | 82.2 → 80.5 | 200 | 90.0 | 82.8 → 80.7 |

the model's performance will be heavily sacrificed despite a substantial number of pruned prototypes.

Fortunately, by using only top- \tilde{M} important ($\tilde{M} = 1, 2, 4, 6, 8$) prototypes per class, our importance-based strategy can greatly prune MGProto, while maintaining a high classification accuracy. Interestingly, discarding 20% of prototypes slightly leads to increased accuracy. With a very large pruning rate (e.g., 90%), our method exhibits a tolerable performance decrease (about 2% in both backbones). This is because the large-prior prototypes always lie in high-density regions of the data distribution (see Fig. 6(b)), capturing enough representative and crucial information. It could be imagined that removing those small-prior prototypes does not render significant changes in the decision boundary.

4.3.4 Interpretability Quantification

Table 7 shows the interpretability results evaluated on CUB. MGProto has the highest consistency score, indicating that the object parts activated by our prototypes are consistent across different images. This is likely because our prototypes are holistically learned from a weighted average of a large set of relevant features, allowing them to consistently capture cross-image semantics. MGProto also achieves competitive stability score. The lowest OIRR score demonstrates that MGProto relies more on the object region and less on the background context to support its classification decision. The DAUC result indicates that MGProto produces interpretations that best influence its classification predictions. We also compute the prototype purity in Table 8, showing that the prototypes produced by our MGProto have a high degree of purity, i.e., each prototype focuses on semantically-consistent object parts among different images.

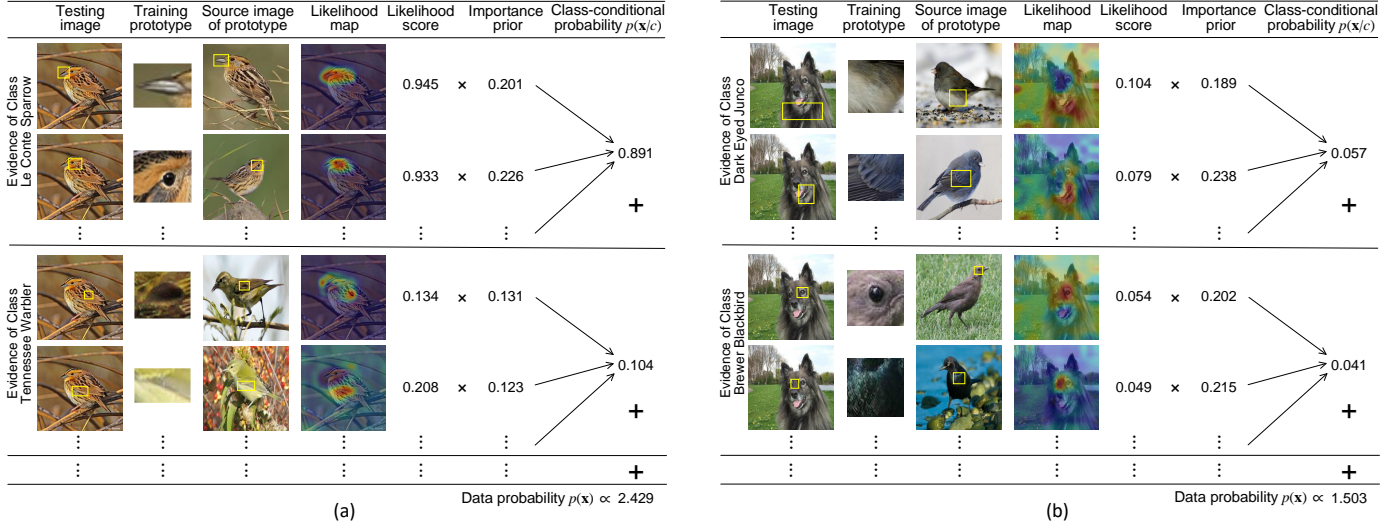


Fig. 8. Interpretable and trustworthy reasoning of our MGProto method for (a) classifying an In-Distribution Le Conte Sparrow image from CUB test set and (b) identifying an Out-of-Distribution Keeshond image from Pets. In the figure, we only show the top-2 classification predictions.

TABLE 7

Quantitative interpretability results (%) on CUB test set using full images, where all models are based on VGG19 backbone.

| Metric | ProtoPNet [10] | Deformable [25] | TesNet [15] | ST-ProtoPNet [18] | SDEA-SA [21] | MGProto (ours) |
|----------------------------|----------------|-----------------|-------------|-------------------|--------------|----------------|
| Consistency (\uparrow) | 45.29 | 57.87 | 60.75 | 74.08 | 80.45 | 93.21 |
| Stability (\uparrow) | 42.23 | 43.91 | 39.20 | 44.96 | 46.30 | 46.95 |
| OIRR (\downarrow) | 37.26 | 28.68 | 38.97 | 28.09 | 33.65 | 22.30 |
| DAUC (\downarrow) | 7.39 | 5.99 | 5.86 | 5.74 | 4.30 | 3.11 |

TABLE 8

Prototype purity (%) on train and test sets of CUB using full images, where all models are based on ResNet50 backbone.

| Method | Purity (train) \uparrow | Purity (test) \uparrow |
|------------------|-----------------------------------|-----------------------------------|
| ProtoPNet [10] | 0.44 \pm 0.21 | 0.46 \pm 0.22 |
| ProtoTree [16] | 0.13 \pm 0.14 | 0.14 \pm 0.16 |
| ProtoPShare [42] | 0.43 \pm 0.21 | 0.43 \pm 0.22 |
| ProtoPool [43] | 0.35 \pm 0.20 | 0.36 \pm 0.21 |
| PIP-Net [17] | 0.63 \pm 0.25 | 0.65 \pm 0.25 |
| MGProto | 0.68 \pm 0.22 | 0.69 \pm 0.22 |

4.4 Ablation Studies

4.4.1 Auxiliary Loss and Prototype Mining

In Table 9, we provide extensive ablation experiments on the auxiliary loss and prototype mining. Firstly, with the use of auxiliary loss \mathcal{L}_{aux} , the classification accuracy is improved, affirming its ability to aid the model backbone in enhancing feature extraction, as in [40]. However, \mathcal{L}_{aux} does not have much effect on the interpretability measures, because it is designed primarily for feature extraction rather than interpretability.

On the other hand, our prototype mining \mathcal{L}_{mn} improves the accuracy since it explicitly enforces the prototypes of MGProto to capture more difficult-to-learn visual features from sub-salient object parts. Additionally, \mathcal{L}_{mn} also enhances interpretability, notably regarding OIRR and DAUC, because \mathcal{L}_{mn} enforces prototypes to activate more sub-salient object regions, as shown in Fig. 9. We notice a marginal improvement of consistency score compared to other metrics. We argue that this is because the prototype learning using \mathcal{L}_{ce} can already acquire highly consistent prototypes across images, by holistically leveraging a large set of relevant features of different samples.

TABLE 9

Ablation analysis of the compared mining loss \mathcal{L}_{mn} in Eq. (10) and auxiliary loss \mathcal{L}_{aux} in Eq. (13) for the proposed MGProto method.

| \mathcal{L}_{ce} | \mathcal{L}_{aux} | \mathcal{L}_{mn} | Accuracy (%) | | | Interpretability (%), V19 | | | |
|--------------------|---------------------|--------------------|--------------|-----------|-----------|---------------------------|-------------------------|----------------------|----------------------|
| | | | CUB(R34) | Dogs(R34) | Cars(R50) | Consist.(\uparrow) | Stability(\uparrow) | OIRR(\downarrow) | DAUC(\downarrow) |
| \checkmark | | | 79.6 | 81.0 | 87.0 | 92.97 | 45.67 | 23.83 | 3.91 |
| \checkmark | \checkmark | | 81.1 | 82.5 | 88.7 | 92.90 | 46.06 | 23.70 | 3.52 |
| \checkmark | | \checkmark | 81.5 | 82.9 | 88.5 | 93.11 | 46.38 | 22.33 | 3.20 |
| \checkmark | \checkmark | \checkmark | 82.2 | 83.6 | 89.2 | 93.21 | 46.95 | 22.30 | 3.11 |

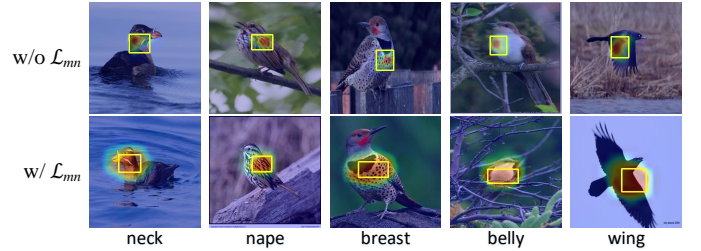


Fig. 9. Visual comparison of prototypes learned without (w/o) and with (w/) prototype mining \mathcal{L}_{mn} , where each column shows prototypes from the same class, representing the same object part. These boxes are all drawn around the largest 5% of values of the activation map.

To explore the generality of our horse-racing based prototype mining strategy, we also apply it to other existing prototypical-part methods, e.g., ProtoPNet, TesNet, and ST-ProtoPNet. Results in Table 10 show that our prototype mining strategy is still effective in these existing models relying on point-based learning techniques. We notice the accuracy improvement is particularly significant in the vanilla ProtoPNet [10], mostly because this baseline model has the worse classification performance among the three models.

TABLE 10

Improved accuracy (%) of existing prototypical-part networks on CUB, integrated with our prototype mining, based on ResNet34 backbone.

| ProtoPNet | | TesNet | | ST-ProtoPNet | |
|--------------|----------|--------------|----------|--------------|----------|
| Vanilla [10] | + Mining | Vanilla [15] | + Mining | Vanilla [12] | + Mining |
| 72.4 | 76.5 | 76.2 | 78.6 | 77.4 | 79.3 |

TABLE 11

Effect of the prototype diversity constraint in Eq. (8) on the within-class distance between prototype means and classification accuracy (%).

| CUB(R34) | | | | Cars(R50) | | | |
|---------------------|------|-------------|------|---------------------|------|-------------|------|
| Closed-form Eq. (7) | | Our Eq. (8) | | Closed-form Eq. (7) | | Our Eq. (8) | |
| Dist. | Acc. | Dist. | Acc. | Dist. | Acc. | Dist. | Acc. |
| 0.0595 | 81.2 | 0.1521 | 82.2 | 0.0746 | 88.3 | 0.1680 | 89.2 |

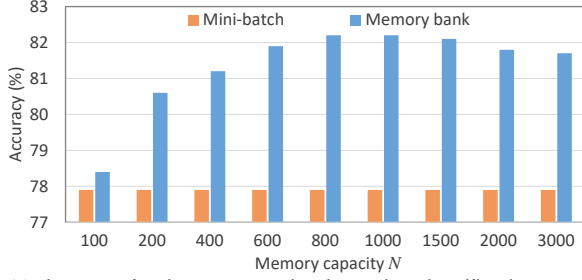


Fig. 10. Impact of using memory bank on the classification accuracy, employing a ResNet34-based MGProto model on the CUB dataset.

4.4.2 Prototype Diversity in M-step

In Eq. (8), we introduce a diversity constraint to improve the within-class distances between prototype means. Table 11 presents an ablation study using full images of CUB and Cars. Our approach in Eq. (8) can significantly increase the average pair-wise distances (L_2) between prototype means. Also, prototypes with greater diversity tend to correlate with higher classification accuracy, in line with findings observed in established methods [15], [25], [46].

4.4.3 Effect of Memory Bank

External memory is used in our MGProto for GMMs to accurately learn the prototype distributions. Here, we study the effect of memory capacity N on the classification accuracy. The result in Fig. 10 shows that the external memory contributes to higher accuracy, compared with the learning from only mini-batch samples. However, a memory with too large capacity evolves too slowly and the presence of early-trained features can deteriorate performance, while a small-capacity memory cannot store enough features for a reliable GMM estimation. Hence, we choose the memory capacity $N = 800$ for CUB (for other datasets we select its values based on the class sample ratio relative to CUB).

4.4.4 T and λ_1 in Prototype Mining

We also investigate the effect of the two important hyperparameters T and λ_1 utilised in our prototype mining approach, with results shown in Fig. 11. It can be seen that when T is greater than 20, the accuracy of MGProto is high and generally stable. For the mining loss weight λ_1 , setting it too low fails to introduce sufficient mining supervision signals, whereas increasing it too much also causes decreased classification accuracy. Therefore, we have $T = 20$ and $\lambda_1 = 0.2$ in all other experiments.

5 DISCUSSION AND LIMITATION

As outlined in Eq. (1) and (14), the existing prototypical-part networks and our MGProto method require to ground

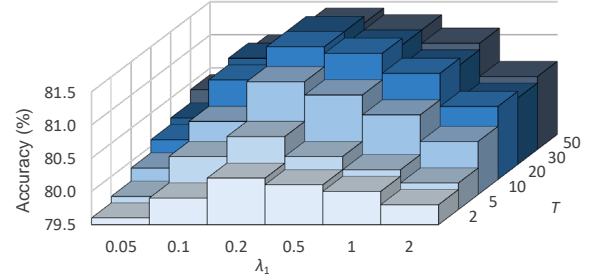


Fig. 11. Effects of T and λ_1 on the classification accuracy of MGProto, evaluated using a ResNet34-based model on CUB.

prototypes in the human-understandable space of training images. This replacement step aims to find the closest feature patch for each prototype by going through all training images periodically at a regular interval during the training process, as shown in Fig. 2. However, this computationally-intensive step can hinder the scalability of these models to datasets with millions of training samples, such as ImageNet [76] that has a large number of classes. Furthermore, the large number of classes may challenge the learning process because prototypes from different classes may become closer to one another, leading to ambiguities in interpretation and an increased risk of misclassification. In this regard, developing more efficient replacement strategy (e.g. ball representation of prototypical concepts in ProtoConcept [45]) and more effective learning algorithm for prototypes is highly desirable in future research.

Our proposed MGProto method leverages class-specific prototypes, which are not shared among classes to ensure clear interpretability for each class. Nevertheless, this approach may face challenges in scenarios involving a large number of classes (e.g., 1000 classes in ImageNet) due to the following two reasons: 1) the number of prototypes scales linearly with the number of classes, making it intractable; and 2) as the number of classes grows, the prototypes will become highly similar to each other and the explanation maps they generate for different classes will start to be nearly identical, thereby significantly reducing interpretability. One potential solution is to incorporate the idea of class-shared prototypes [42], [43], which partially merges prototypes for those classes with similar features. By sharing prototypes between classes, we can address scalability (it becomes sublinear in the number of classes) and interpretability (we have many shared prototypes and a few specific prototypes that are more interpretable for each class). We argue that this adaptation can be straightforwardly implemented in our method, by making some GMM components shared across related classes.

Our MGProto method evaluates the model interpretability using objective metrics in Table 7 and Table 8. Another possibility to assess the interpretability relies on user studies [45], [102], which directly gauge how intuitive the explanations appear to human users. To enhance our evaluation, we plan to conduct user-based experiments for our proposed method in the future. Additionally, considering that our prototypes are learned to model the underlying data distributions, it is possible to sample from the distributions and generate new examples for counterfactual explanations. We plan to also explore this in future study.

6 CONCLUSION

This work presented MGProto, a generative learning paradigm to produce mixtures of Gaussian-distributed prototypes for interpretable and trustworthy image recognition. Different from current point-based prototype learning models, MGProto naturally mitigates the performance degradation caused by the projection of point-based learned prototypes, and effectively recognises OoD inputs to ensure decision trustworthiness. Additionally, a novel and generic strategy is proposed to enhance the prototype learning by mining from less-salient object parts, inspired by the classic legend of Tian Ji's horse-racing. MGProto can be substantially compressed via an importance-based pruning strategy, while still keeping high classification accuracy. Experimentally, the proposed method obtains SOTA performances on interpretable image recognition, OoD detection, and interpretability quantification. A series of ablation studies are also performed to validate the significance of our key claims and effectiveness of the critical model designs.

ACKNOWLEDGEMENTS

This work was supported by funding from the Australian Government under the Medical Research Future Fund - Grant MRFAI000090 for the Transforming Breast Cancer Screening with Artificial Intelligence (BRAIx) Project. G. Carneiro acknowledges the support by the Engineering and Physical Sciences Research Council (EPSRC) through grant EP/Y018036/1. The authors would like to thank the editor and the anonymous reviewers for their valuable comments and suggestions.

REFERENCES

- [1] A. Krizhevsky, I. Sutskever, and G. E. Hinton, "Imagenet classification with deep convolutional neural networks," *Communications of the ACM*, vol. 60, no. 6, pp. 84–90, 2017. [1](#)
- [2] Y. LeCun, Y. Bengio, and G. Hinton, "Deep learning," *Nature*, vol. 521, no. 7553, pp. 436–444, 2015. [1](#)
- [3] C. Rudin, "Stop explaining black box machine learning models for high stakes decisions and use interpretable models instead," *Nature Machine Intelligence*, vol. 1, no. 5, pp. 206–215, 2019. [1, 3](#)
- [4] E. Tjoo and C. Guan, "A survey on explainable artificial intelligence (xai): Toward medical xai," *IEEE Transactions on Neural Networks and Learning Systems*, vol. 32, no. 11, pp. 4793–4813, 2020. [1](#)
- [5] H. M. Frazer, C. A. Peña-Solorzano, C. F. Kwok, M. S. Elliott, Y. Chen, C. Wang, B. T. A.-Q. O. . F. S. K. . H. B. . K. R. . K. K. . L. S. . M. E. . . N. T. L. . R. P. B. . S. D. . . W. P. C. 9, J. F. Lippey, J. L. Hopper, P. Brothie, *et al.*, "Comparison of ai-integrated pathways with human-ai interaction in population mammographic screening for breast cancer," *Nature Communications*, vol. 15, no. 1, p. 7525, 2024. [1](#)
- [6] J. Kim and J. Canny, "Interpretable learning for self-driving cars by visualizing causal attention," in *Proceedings of the IEEE International Conference on Computer Vision*, pp. 2942–2950, 2017. [1](#)
- [7] C. Wang, Z. Cui, J. Yang, M. Han, G. Carneiro, and D. Shen, "Bowlnet: Joint semantic-geometric ensemble learning for bowel segmentation from both partially and fully labeled ct images," *IEEE Transactions on Medical Imaging*, vol. 42, no. 4, pp. 1225–1236, 2022. [1](#)
- [8] P. W. Koh and P. Liang, "Understanding black-box predictions via influence functions," in *International Conference on Machine Learning*, pp. 1885–1894, PMLR, 2017. [1](#)
- [9] D. Alvarez Melis and T. Jaakkola, "Towards robust interpretability with self-explaining neural networks," *Advances in Neural Information Processing Systems*, vol. 31, 2018. [1](#)
- [10] C. Chen, O. Li, D. Tao, A. Barnett, C. Rudin, and J. K. Su, "This looks like that: deep learning for interpretable image recognition," *Advances in Neural Information Processing Systems*, vol. 32, 2019. [1, 2, 3, 4, 5, 8, 9, 10, 11](#)
- [11] M. Böhle, M. Fritz, and B. Schiele, "B-cos networks: Alignment is all we need for interpretability," in *Proceedings of the IEEE/CVF Conference on Computer Vision and Pattern Recognition*, pp. 10329–10338, 2022. [1](#)
- [12] C. Wang, Y. Chen, F. Liu, M. Elliott, C. F. Kwok, C. Peña-Solorzano, H. Frazer, D. J. McCarthy, and G. Carneiro, "An interpretable and accurate deep-learning diagnosis framework modelled with fully and semi-supervised reciprocal learning," *IEEE Transactions on Medical Imaging*, 2023. [1, 4, 11](#)
- [13] A. Aamodt and E. Plaza, "Case-based reasoning: Foundational issues, methodological variations, and system approaches," *AI Communications*, vol. 7, no. 1, pp. 39–59, 1994. [1](#)
- [14] Y. Yang, Y. Zhuang, and Y. Pan, "Multiple knowledge representation for big data artificial intelligence: framework, applications, and case studies," *Frontiers of Information Technology & Electronic Engineering*, vol. 22, no. 12, pp. 1551–1558, 2021. [1](#)
- [15] J. Wang, H. Liu, X. Wang, and L. Jing, "Interpretable image recognition by constructing transparent embedding space," in *Proceedings of the IEEE/CVF International Conference on Computer Vision*, pp. 895–904, 2021. [1, 2, 3, 4, 5, 9, 11, 12](#)
- [16] M. Nauta, R. van Bree, and C. Seifert, "Neural prototype trees for interpretable fine-grained image recognition," in *Proceedings of the IEEE/CVF Conference on Computer Vision and Pattern Recognition*, pp. 14933–14943, 2021. [1, 3, 8, 9, 11](#)
- [17] M. Nauta, J. Schlöterer, M. van Keulen, and C. Seifert, "Pip-net: Patch-based intuitive prototypes for interpretable image classification," in *Proceedings of the IEEE/CVF Conference on Computer Vision and Pattern Recognition*, pp. 2744–2753, 2023. [1, 3, 5, 8, 9, 11](#)
- [18] C. Wang, Y. Liu, Y. Chen, F. Liu, Y. Tian, D. McCarthy, H. Frazer, and G. Carneiro, "Learning support and trivial prototypes for interpretable image classification," in *Proceedings of the IEEE/CVF International Conference on Computer Vision*, pp. 2062–2072, 2023. [1, 2, 3, 4, 5, 8, 9, 11](#)
- [19] J. Bernardo, M. Bayarri, J. Berger, A. Dawid, D. Heckerman, A. Smith, and M. West, "Generative or discriminative? getting the best of both worlds," *Bayesian Statistics*, vol. 8, no. 3, pp. 3–24, 2007. [1, 2](#)
- [20] Z. Carmichael, S. Lohit, A. Cherian, M. J. Jones, and W. J. Scheirer, "Pixel-grounded prototypical part networks," in *Proceedings of the IEEE/CVF Winter Conference on Applications of Computer Vision*, pp. 4768–4779, 2024. [2, 4](#)
- [21] Q. Huang, M. Xue, W. Huang, H. Zhang, J. Song, Y. Jing, and M. Song, "Evaluation and improvement of interpretability of self-explainable part-prototype networks," in *Proceedings of the IEEE/CVF International Conference on Computer Vision*, pp. 2011–2020, 2023. [2, 3, 5, 8, 9, 11](#)
- [22] M. Xue, Q. Huang, H. Zhang, L. Cheng, J. Song, M. Wu, and M. Song, "Protopformer: Concentrating on prototypical parts in vision transformers for interpretable image recognition," *arXiv preprint arXiv:2208.10431*, 2022. [2, 3](#)
- [23] S. Gautam, A. Boubekki, S. Hansen, S. Salahuddin, R. Jenssen, M. Höhne, and M. Kampffmeyer, "Protovae: A trustworthy self-explainable prototypical variational model," *Advances in Neural Information Processing Systems*, vol. 35, pp. 17940–17952, 2022. [2](#)
- [24] S. Kim, J. Nam, and B. C. Ko, "Vit-net: Interpretable vision transformers with neural tree decoder," in *International Conference on Machine Learning*, pp. 11162–11172, PMLR, 2022. [2, 3](#)
- [25] J. Donnelly, A. J. Barnett, and C. Chen, "Deformable protopnet: An interpretable image classifier using deformable prototypes," in *Proceedings of the IEEE/CVF Conference on Computer Vision and Pattern Recognition*, pp. 10265–10275, 2022. [2, 3, 4, 5, 8, 9, 11, 12](#)
- [26] R. Mackowiak, L. Ardizzone, U. Kothe, and C. Rother, "Generative classifiers as a basis for trustworthy image classification," in *Proceedings of the IEEE/CVF Conference on Computer Vision and Pattern Recognition*, pp. 2971–2981, 2021. [2](#)
- [27] J. Serrà, D. Álvarez, V. Gómez, O. Slizovskaia, J. F. Núñez, and J. Luque, "Input complexity and out-of-distribution detection with likelihood-based generative models," in *International Conference on Learning Representations*, pp. 1–10, 2020. [2](#)
- [28] A. Ng and M. Jordan, "On discriminative vs. generative classifiers: A comparison of logistic regression and naive bayes," *Advances in Neural Information Processing Systems*, vol. 14, 2001. [2](#)

- [29] J.-J. Shu, "On generalized tian ji's horse racing strategy," *Interdisciplinary Science Reviews*, vol. 37, no. 2, pp. 187–193, 2012. [2](#), [3](#), [6](#)
- [30] K. Simonyan, A. Vedaldi, and A. Zisserman, "Deep inside convolutional networks: Visualising image classification models and saliency maps," *arXiv preprint arXiv:1312.6034*, 2013. [2](#)
- [31] M. D. Zeiler and R. Fergus, "Visualizing and understanding convolutional networks," in *European Conference on Computer Vision*, pp. 818–833, Springer, 2014. [2](#)
- [32] R. R. Selvaraju, M. Cogswell, A. Das, R. Vedantam, D. Parikh, and D. Batra, "Grad-cam: Visual explanations from deep networks via gradient-based localization," in *Proceedings of the IEEE International Conference on Computer Vision*, pp. 618–626, 2017. [2](#)
- [33] L. Fang, C. Wang, S. Li, H. Rabbani, X. Chen, and Z. Liu, "Attention to lesion: Lesion-aware convolutional neural network for retinal optical coherence tomography image classification," *IEEE Transactions on Medical Imaging*, vol. 38, no. 8, pp. 1959–1970, 2019. [2](#)
- [34] S. M. Lundberg and S.-I. Lee, "A unified approach to interpreting model predictions," *Advances in Neural Information Processing Systems*, vol. 30, 2017. [2](#)
- [35] Q. Zhang, R. Cao, F. Shi, Y. N. Wu, and S.-C. Zhu, "Interpreting cnn knowledge via an explanatory graph," in *Proceedings of the AAAI Conference on Artificial Intelligence*, vol. 32, 2018. [2](#)
- [36] V. Shitole, F. Li, M. Kahng, P. Tadepalli, and A. Fern, "One explanation is not enough: structured attention graphs for image classification," *Advances in Neural Information Processing Systems*, vol. 34, pp. 11352–11363, 2021. [2](#)
- [37] Y. Goyal, Z. Wu, J. Ernst, D. Batra, D. Parikh, and S. Lee, "Counterfactual visual explanations," in *International Conference on Machine Learning*, pp. 2376–2384, PMLR, 2019. [2](#)
- [38] D. Teney, E. Abbasnedjad, and A. v. d. Hengel, "Learning what makes a difference from counterfactual examples and gradient supervision," in *European Conference on Computer Vision*, pp. 580–599, Springer, 2020. [2](#)
- [39] E. M. Kenny and M. T. Keane, "On generating plausible counterfactual and semi-factual explanations for deep learning," in *Proceedings of the AAAI Conference on Artificial Intelligence*, vol. 35, pp. 11575–11585, 2021. [2](#)
- [40] Y. Ukai, T. Hirakawa, T. Yamashita, and H. Fujiyoshi, "This looks like it rather than that: Protoknn for similarity-based classifiers," in *International Conference on Learning Representations*, 2023. [3](#), [7](#), [8](#), [9](#), [11](#)
- [41] M. Keswani, S. Ramakrishnan, N. Reddy, and V. N. Balasubramanian, "Proto2proto: Can you recognize the car, the way i do?," in *Proceedings of the IEEE/CVF Conference on Computer Vision and Pattern Recognition*, pp. 10233–10243, 2022. [3](#)
- [42] D. Rymarczyk, Ł. Struski, J. Tabor, and B. Zieliński, "Protop-share: Prototypical parts sharing for similarity discovery in interpretable image classification," in *Proceedings of the ACM SIGKDD Conference on Knowledge Discovery & Data Mining*, pp. 1420–1430, 2021. [3](#), [8](#), [10](#), [11](#), [12](#)
- [43] D. Rymarczyk, Ł. Struski, M. Górszczak, K. Lewandowska, J. Tabor, and B. Zieliński, "Interpretable image classification with differentiable prototypes assignment," in *European Conference on Computer Vision*, pp. 351–368, Springer, 2022. [3](#), [4](#), [8](#), [9](#), [11](#), [12](#)
- [44] A. Bontempelli, S. Teso, K. Tentori, F. Giunchiglia, and A. Passerini, "Concept-level debugging of part-prototype networks," in *International Conference on Learning Representations*, 2023. [3](#), [8](#)
- [45] C. Ma, B. Zhao, C. Chen, and C. Rudin, "This looks like those: Illuminating prototypical concepts using multiple visualizations," *Advances in Neural Information Processing Systems*, vol. 36, 2024. [3](#), [9](#), [12](#)
- [46] C. Wang, Y. Chen, Y. Liu, Y. Tian, F. Liu, D. J. McCarthy, M. Elliott, H. Frazer, and G. Carneiro, "Knowledge distillation to ensemble global and interpretable prototype-based mammogram classification models," in *International Conference on Medical Image Computing and Computer-Assisted Intervention*, pp. 14–24, 2022. [3](#), [12](#)
- [47] C. Wang, F. Liu, Y. Chen, H. Frazer, and G. Carneiro, "Cross- and intra-image prototypical learning for multi-label disease diagnosis and interpretation," *IEEE Transactions on Medical Imaging*, 2025. [3](#)
- [48] M. Gerstenberger, S. Maaß, P. Eisert, and S. Bosse, "A differentiable gaussian prototype layer for explainable fruit segmentation," in *IEEE International Conference on Image Processing (ICIP)*, pp. 2665–2669, IEEE, 2023. [3](#)
- [49] H. Wu, C. Wang, L. Mei, T. Yang, M. Zhu, D. Shen, and Z. Cui, "Cephalometric landmark detection across ages with prototypical network," in *International Conference on Medical Image Computing and Computer-Assisted Intervention*, pp. 155–165, Springer, 2024. [3](#)
- [50] C. Wang, F. Liu, Y. Chen, C. F. Kwok, M. Elliott, C. Pena-Solorzano, D. J. McCarthy, H. Frazer, and G. Carneiro, "Progressive mining and dynamic distillation of hierarchical prototypes for disease classification and localisation," *IEEE Journal of Biomedical and Health Informatics*, 2025. [3](#)
- [51] D. A. Reynolds et al., "Gaussian mixture models," *Encyclopedia of Biometrics*, vol. 741, no. 659–663, 2009. [3](#), [5](#), [6](#)
- [52] L. Wu, Z. Zhong, L. Fang, X. He, Q. Liu, J. Ma, and H. Chen, "Sparsely annotated semantic segmentation with adaptive gaussian mixtures," in *Proceedings of the IEEE/CVF Conference on Computer Vision and Pattern Recognition*, pp. 15454–15464, 2023. [3](#)
- [53] C. Liang, W. Wang, J. Miao, and Y. Yang, "Gmmseg: Gaussian mixture based generative semantic segmentation models," *Advances in Neural Information Processing Systems*, vol. 35, pp. 31360–31375, 2022. [3](#)
- [54] W. Yuan, B. Eckart, K. Kim, V. Jampani, D. Fox, and J. Kautz, "Deepgmr: Learning latent gaussian mixture models for registration," in *European Conference on Computer Vision*, pp. 733–750, Springer, 2020. [3](#)
- [55] Z. Cheng, H. Sun, M. Takeuchi, and J. Katto, "Learned image compression with discretized gaussian mixture likelihoods and attention modules," in *Proceedings of the IEEE/CVF Conference on Computer Vision and Pattern Recognition*, pp. 7939–7948, 2020. [3](#)
- [56] Z. Xie, T. He, S. Tian, Y. Fu, J. Zhou, and D. Chen, "Joint gaussian mixture model for versatile deep visual model explanation," *Knowledge-Based Systems*, vol. 280, p. 110989, 2023. [3](#)
- [57] T. K. Moon, "The expectation-maximization algorithm," *IEEE Signal Processing Magazine*, vol. 13, no. 6, pp. 47–60, 1996. [3](#), [5](#)
- [58] L. Wang, C. Goursaud, N. Nikaein, L. Cottatellucci, and J.-M. Gorce, "Cooperative scheduling for coexisting body area networks," *IEEE Transactions on Wireless Communications*, vol. 12, no. 1, pp. 123–133, 2012. [3](#)
- [59] M. Leng and M. Parlar, "Game-theoretic analysis of an ancient chinese horse race problem," *Computers & Operations Research*, vol. 33, no. 7, pp. 2033–2055, 2006. [3](#)
- [60] A. Estabrooks, T. Jo, and N. Japkowicz, "A multiple resampling method for learning from imbalanced data sets," *Computational intelligence*, vol. 20, no. 1, pp. 18–36, 2004. [5](#)
- [61] J. Pearl, *Probabilistic reasoning in intelligent systems: networks of plausible inference*. Morgan kaufmann, 1988. [5](#)
- [62] I. Rish et al., "An empirical study of the naive bayes classifier," in *IJCAI Workshop on Empirical Methods in Artificial Intelligence*, vol. 3, pp. 41–46, 2001. [5](#)
- [63] F. Peng, D. Schuurmans, and S. Wang, "Augmenting naive bayes classifiers with statistical language models," *Information Retrieval*, vol. 7, pp. 317–345, 2004. [5](#)
- [64] W. Liu, X. Wang, J. Owens, and Y. Li, "Energy-based out-of-distribution detection," *Advances in Neural Information Processing Systems*, vol. 33, pp. 21464–21475, 2020. [5](#), [10](#)
- [65] T. Chen, S. Kornblith, M. Norouzi, and G. Hinton, "A simple framework for contrastive learning of visual representations," in *International Conference on Machine Learning*, pp. 1597–1607, PMLR, 2020. [5](#)
- [66] J. Fan and Z. Zhang, "Memory-based cross-image contexts for weakly supervised semantic segmentation," *IEEE transactions on Pattern Analysis and Machine Intelligence*, vol. 45, no. 5, pp. 6006–6020, 2022. [5](#)
- [67] J. Kwok and R. P. Adams, "Priors for diversity in generative latent variable models," *Advances in Neural Information Processing Systems*, vol. 25, 2012. [6](#)
- [68] S. Kim, D. Kim, M. Cho, and S. Kwak, "Proxy anchor loss for deep metric learning," in *Proceedings of the IEEE/CVF Conference on Computer Vision and Pattern Recognition*, pp. 3238–3247, 2020. [7](#)
- [69] F. Doshi-Velez and B. Kim, "Towards a rigorous science of interpretable machine learning," *arXiv preprint arXiv:1702.08608*, 2017. [8](#)
- [70] C. Wah, S. Branson, P. Welinder, P. Perona, and S. Belongie, "The caltech-ucsd birds-200-2011 dataset," 2011. [8](#)

- [71] J. Krause, M. Stark, J. Deng, and L. Fei-Fei, "3d object representations for fine-grained categorization," in *Proceedings of the IEEE International Conference on Computer Vision Workshops*, pp. 554–561, 2013. [8](#)
- [72] A. Khosla, N. Jayadevaprakash, B. Yao, and F.-F. Li, "Novel dataset for fine-grained image categorization: Stanford dogs," in *Proc. CVPR Workshop on Fine-grained Visual Categorization (FGVC)*, vol. 2, 2011. [8](#)
- [73] O. M. Parkhi, A. Vedaldi, A. Zisserman, and C. Jawahar, "Cats and dogs," in *IEEE Conference on Computer Vision and Pattern Recognition*, pp. 3498–3505, IEEE, 2012. [8](#)
- [74] S. Lapuschkin, A. Binder, G. Montavon, K.-R. Muller, and W. Samek, "Analyzing classifiers: Fisher vectors and deep neural networks," in *Proceedings of the IEEE Conference on Computer Vision and Pattern Recognition*, pp. 2912–2920, 2016. [8](#)
- [75] V. Petsiuk, A. Das, and K. Saenko, "Rise: Randomized input sampling for explanation of black-box models," *arXiv preprint arXiv:1806.07421*, 2018. [8](#)
- [76] J. Deng, W. Dong, R. Socher, L.-J. Li, K. Li, and L. Fei-Fei, "Imagenet: A large-scale hierarchical image database," in *IEEE Conference on Computer Vision and Pattern Recognition*, pp. 248–255, Ieee, 2009. [8](#), [12](#)
- [77] G. Van Horn, O. Mac Aodha, Y. Song, Y. Cui, C. Sun, A. Shepard, H. Adam, P. Perona, and S. Belongie, "The inaturalist species classification and detection dataset," in *Proceedings of the IEEE Conference on Computer Vision and Pattern Recognition*, pp. 8769–8778, 2018. [8](#)
- [78] A. Paszke, S. Gross, F. Massa, A. Lerer, J. Bradbury, G. Chanan, T. Killeen, Z. Lin, N. Gimelshein, L. Antiga, et al., "Pytorch: An imperative style, high-performance deep learning library," *Advances in Neural Information Processing Systems*, vol. 32, 2019. [8](#)
- [79] J. S. Hunter, "The exponentially weighted moving average," *Journal of Quality Technology*, vol. 18, no. 4, pp. 203–210, 1986. [8](#)
- [80] S. F. Chen and J. Goodman, "An empirical study of smoothing techniques for language modeling," *Computer Speech & Language*, vol. 13, no. 4, pp. 359–394, 1999. [8](#)
- [81] D. Valcarce, J. Parapar, and Á. Barreiro, "Additive smoothing for relevance-based language modelling of recommender systems," in *Proceedings of the Spanish Conference on Information Retrieval*, pp. 1–8, 2016. [8](#)
- [82] S. Basart, M. Mantas, M. Mohammadreza, S. Jacob, and S. Dawn, "Scaling out-of-distribution detection for real-world settings," in *International Conference on Machine Learning*, 2022. [10](#)
- [83] K. Lee, K. Lee, H. Lee, and J. Shin, "A simple unified framework for detecting out-of-distribution samples and adversarial attacks," *Advances in neural information processing systems*, vol. 31, 2018. [10](#)
- [84] Y. Sun, Y. Ming, X. Zhu, and Y. Li, "Out-of-distribution detection with deep nearest neighbors," in *International Conference on Machine Learning*, pp. 20827–20840, PMLR, 2022. [10](#)
- [85] P. Morteza and Y. Li, "Provable guarantees for understanding out-of-distribution detection," in *Proceedings of the AAAI Conference on Artificial Intelligence*, vol. 36, pp. 7831–7840, 2022. [10](#)
- [86] B. Peng, Y. Luo, Y. Zhang, Y. Li, and Z. Fang, "Conjnorm: Tractable density estimation for out-of-distribution detection," in *International Conference on Learning Representations*, 2024. [10](#)
- [87] D. Hendrycks, M. Mazeika, and T. Dietterich, "Deep anomaly detection with outlier exposure," in *International Conference on Learning Representations*, 2019. [10](#)
- [88] L. Tao, X. Du, X. Zhu, and Y. Li, "Non-parametric outlier synthesis," in *International Conference on Learning Representations*, 2023. [10](#)
- [89] Y. Liu, C. X. Tian, H. Li, L. Ma, and S. Wang, "Neuron activation coverage: Rethinking out-of-distribution detection and generalization," in *International Conference on Learning Representations*, 2024. [10](#)
- [90] A. Krizhevsky, G. Hinton, et al., "Learning multiple layers of features from tiny images," 2009. [10](#)
- [91] Y. Netzer, T. Wang, A. Coates, A. Bissacco, B. Wu, A. Y. Ng, et al., "Reading digits in natural images with unsupervised feature learning," in *NIPS workshop on deep learning and unsupervised feature learning*, vol. 2011, p. 4, Granada, 2011. [10](#)
- [92] B. Zhou, A. Lapedriza, A. Khosla, A. Oliva, and A. Torralba, "Places: A 10 million image database for scene recognition," *IEEE transactions on pattern analysis and machine intelligence*, vol. 40, no. 6, pp. 1452–1464, 2017. [10](#)
- [93] F. Yu, A. Seff, Y. Zhang, S. Song, T. Funkhouser, and J. Xiao, "Lsun: Construction of a large-scale image dataset using deep learning with humans in the loop," *arXiv preprint arXiv:1506.03365*, 2015. [10](#)
- [94] P. Xu, K. A. Ehinger, Y. Zhang, A. Finkelstein, S. R. Kulkarni, and J. Xiao, "Turkergaze: Crowdsourcing saliency with webcam based eye tracking," *arXiv preprint arXiv:1504.06755*, 2015. [10](#)
- [95] M. Cimpoi, S. Maji, I. Kokkinos, S. Mohamed, and A. Vedaldi, "Describing textures in the wild," in *Proceedings of the IEEE conference on computer vision and pattern recognition*, pp. 3606–3613, 2014. [10](#)
- [96] D. Hendrycks and K. Gimpel, "A baseline for detecting misclassified and out-of-distribution examples in neural networks," in *International Conference on Learning Representations*, 2017. [10](#)
- [97] S. Liang, Y. Li, and R. Srikant, "Enhancing the reliability of out-of-distribution image detection in neural networks," in *International Conference on Learning Representations*, 2018. [10](#)
- [98] H. Wang, Z. Li, L. Feng, and W. Zhang, "Vim: Out-of-distribution with virtual-logit matching," in *Proceedings of the IEEE/CVF conference on computer vision and pattern recognition*, pp. 4921–4930, 2022. [10](#)
- [99] Y. Sun, C. Guo, and Y. Li, "React: Out-of-distribution detection with rectified activations," *Advances in Neural Information Processing Systems*, vol. 34, pp. 144–157, 2021. [10](#)
- [100] A. Djuricic, N. Bozanic, A. Ashok, and R. Liu, "Extremely simple activation shaping for out-of-distribution detection," in *International Conference on Learning Representations*, 2023. [10](#)
- [101] X. Liu, Y. Lochman, and C. Zach, "Gen: Pushing the limits of softmax-based out-of-distribution detection," in *Proceedings of the IEEE/CVF Conference on Computer Vision and Pattern Recognition*, pp. 23946–23955, 2023. [10](#)
- [102] S. S. Kim, N. Meister, V. V. Ramaswamy, R. Fong, and O. Russakovsky, "Hive: Evaluating the human interpretability of visual explanations," in *European Conference on Computer Vision*, pp. 280–298, Springer, 2022. [12](#)